Supporting Information

Photo-induced hole hopping through tryptophans in proteins

Stanislav Záliš[a,*], Jan Heyda[a,b], Filip Šebesta[c], Jay R. Winkler[d], Harry B. Gray[d,*], Antonín Vlček[a,c,*]

[a] J. Heyrovský Institute of Physical Chemistry, Academy of Sciences of the Czech Republic, Dolejškova 3, CZ-182 23 Prague, Czech Republic
[b] Department of Physical Chemistry, University of Chemistry and Technology, Prague, Technická 5, CZ-166 28 Prague, Czech Republic
[c] School of Biological and Chemical Sciences, Queen Mary University of London, Mile End Road, London E1 4NS, United Kingdom
[d] Beckman Institute, California Institute of Technology, Pasadena, California 91125, United States

Contents

S1. MM trajectories and UV-vis spectroscopic parameter validation

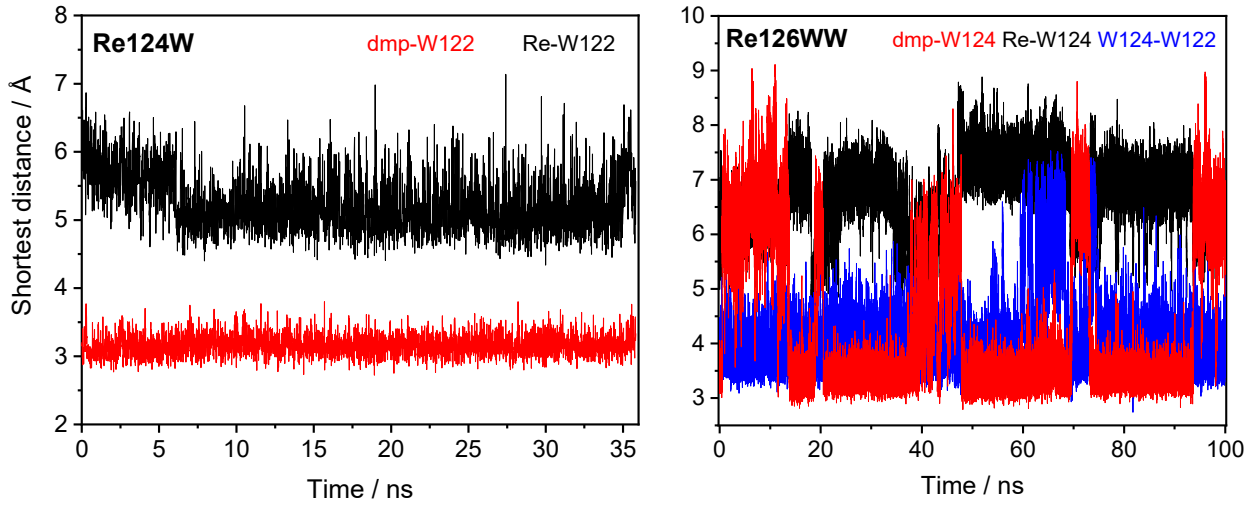

Fig. S1. Classical MM/MD trajectories of the shortest C–C or Re–C cofactor distances in ground-state **Re124W** (left) and **Re126WW** (right). Red: dmp-indole; black: Re-indole; blue: indole-indole. Simulated solution structures are close to crystal structures where Re-W and dmp-W shortest distances of 6.3, 3.4 Å (**Re124WCu^{II}**; PDB: 2I7O) and 6.9, 3.5 Å (**Re122WWCu^{II}**; 6MJS) were determined (1, 2). Periods of long dmp-W124 distances in **Re126WW** correspond to the "distant" conformation where the Re complex rotated around the Re-N(H126) bond, placing dmp away from the W124 indole. The distant conformation was not found for **Re124W**.

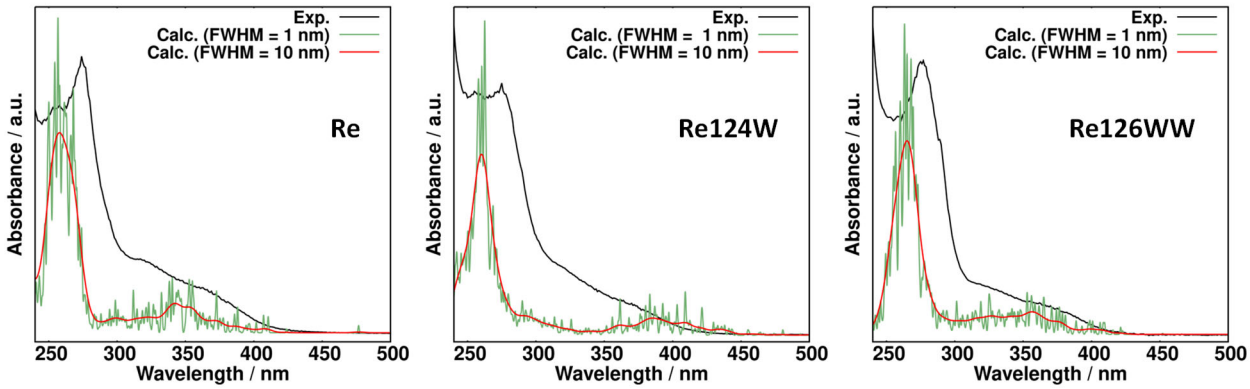

Fig. S2. Experimental and calculated UV-vis spectra of $[Re(im)(CO)_3(dmp)]^+$ in water (Re, left), **Re124W** (middle) and **Re126WW** (right). The calculated spectra were obtained using TDDFT at the PBE0-GD3BJ/6-31+G(d)/SDD level and averaged over 40 snapshots taken from MM/MD trajectories. For **Re124W** and **Re126WW**, the whole QM part (Fig. 1) was considered in TDDFT calculations and the surroundings (solution and the rest of the protein) were included within the electrostatic interaction as point charges taken from MM simulations. 60 lowest singlet excited states were determined for each geometry. 1 or 10 nm Gaussian broadening was applied for averaged spectra.

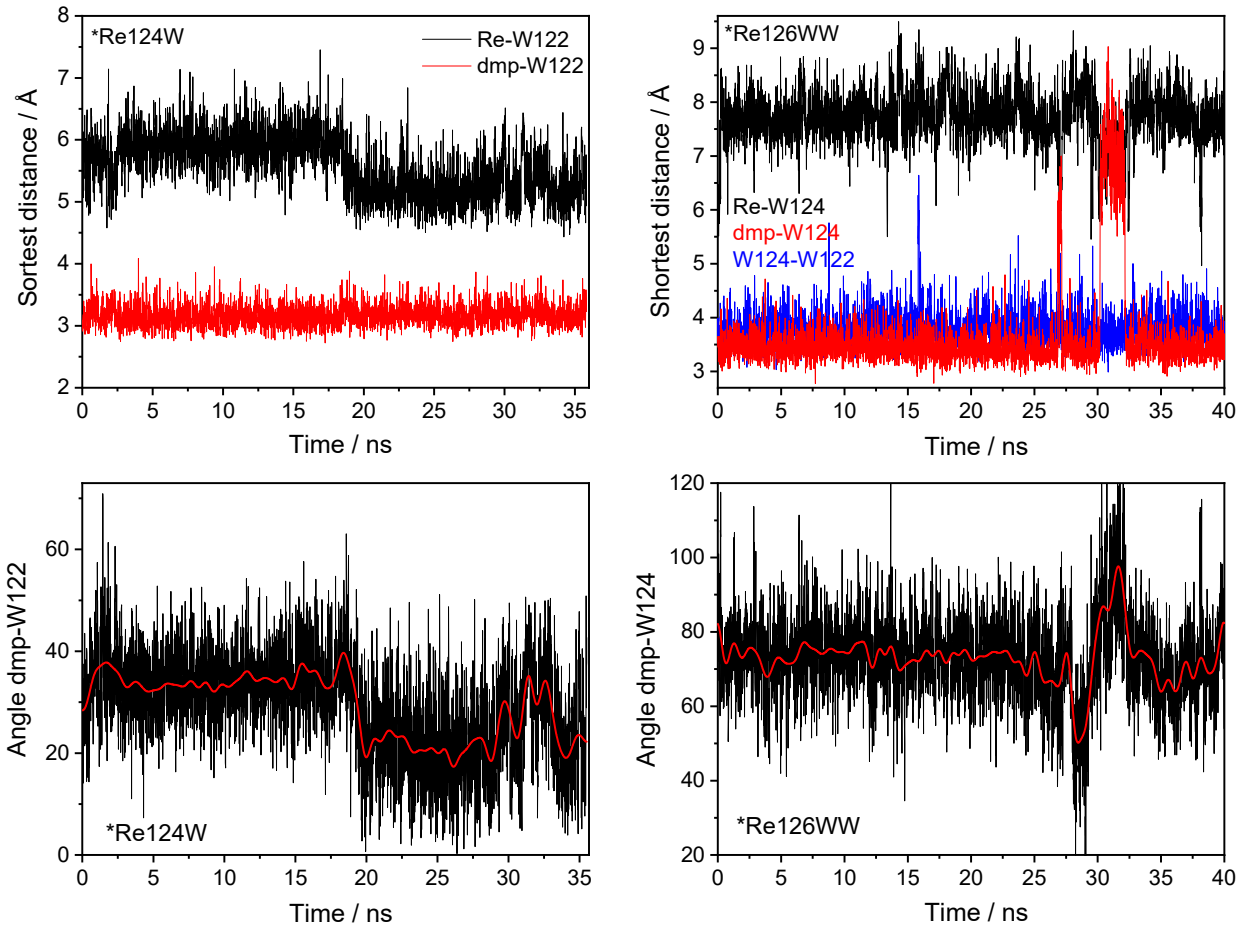

Fig. S3. Classical MM/MD trajectories of the shortest C–C or Re–C cofactor distances (top) and dmp – proximal indole angles (bottom) calculated using MM parametrization for the *Re state of **Re124W** (left) and **Re126WW** (right). The red curves in the lower panels show smoothed trajectories (40 point FFT).

S2. *Re character and UKS spin and charge trajectories

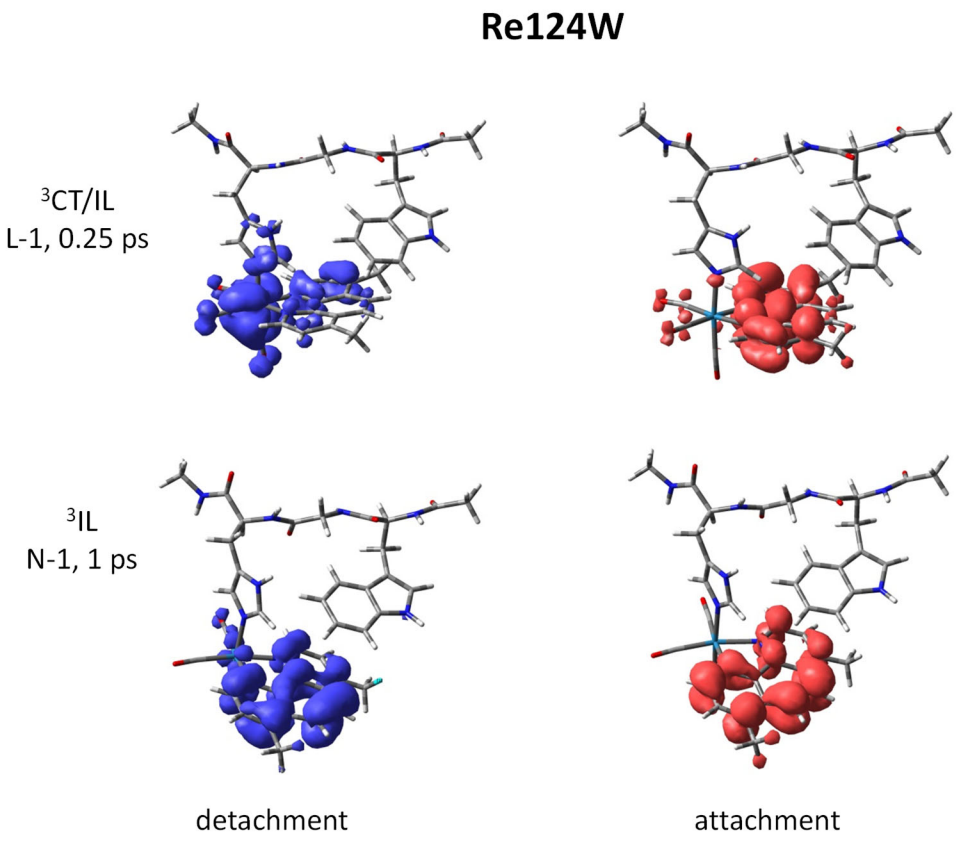

Fig. S4a. Visualization of predominantly ^{3}CT/IL (top row) and ^{3}IL situations (bottom row) of the *Re state in **Re124W** state using electron detachment and attachment densities (3). Calculated by TDDFT at specified snapshots using the Q-Chem software. The two situations differ mainly in the hole localization (blue) while the excited electron is in both cases localized at dmp (red). Typically, *Re is a combination of these two limiting situations. "Pure" ^{3}CT was not observed at any of the calculated trajectories.

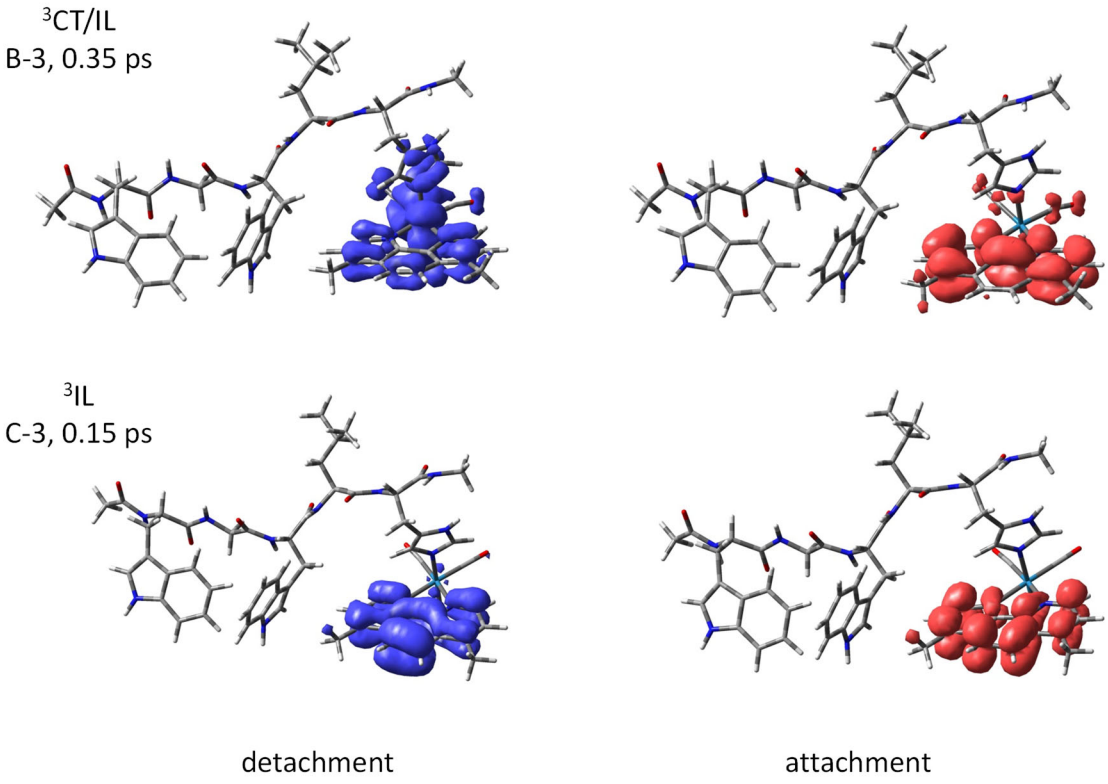

Fig. S4b. Visualization of predominantly ^{3}CT/IL (top row) and ^{3}IL situations (bottom row) of the *Re state in **Re126WW** state using electron detachment and attachment densities (3). Calculated by TDDFT at specified snapshots using the Q-Chem software. The two situations differ mainly in the hole localization (blue) while the excited electron is in both cases localized at dmp (red). Typically, *Re is a combination of these two limiting situations. "Pure" ^{3}CT was not observed at any of the calculated trajectories.

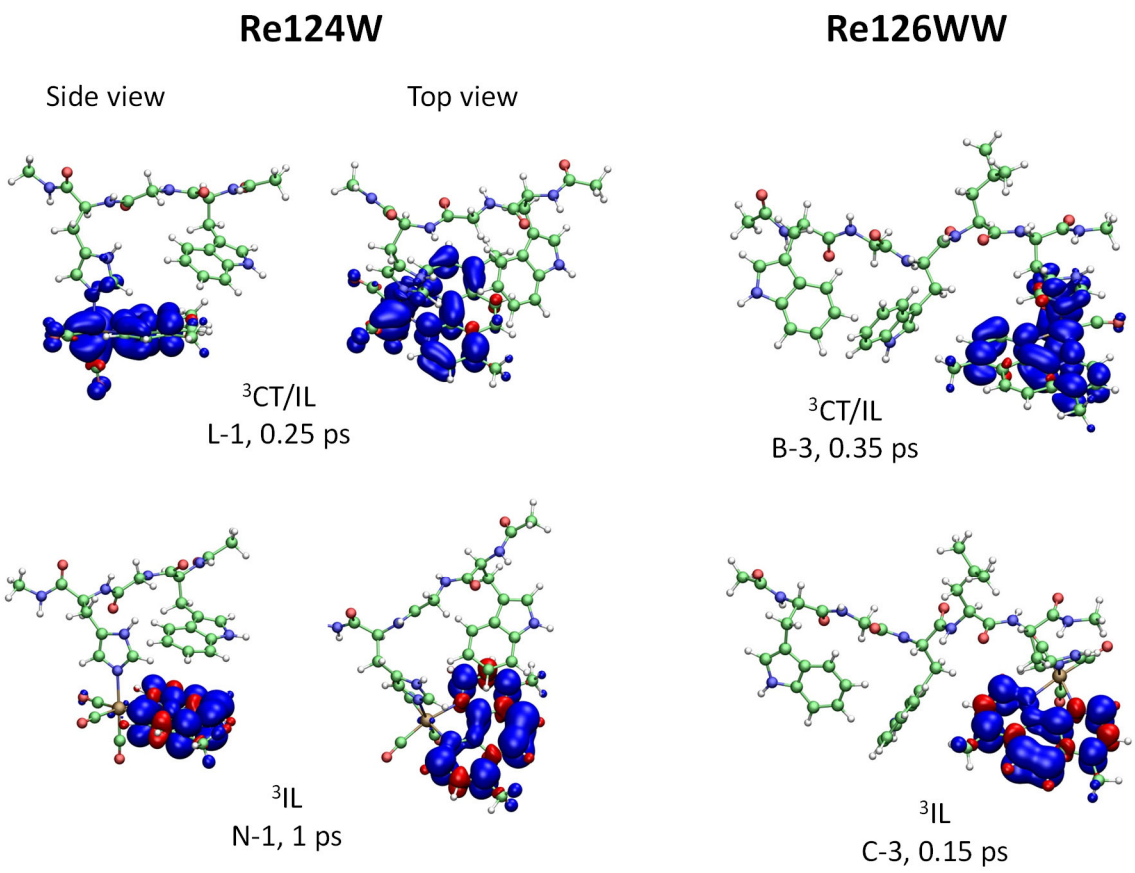

Fig. S4c. Visualization of predominantly ^{3}CT/IL (top row) and ^{3}IL situations (bottom row) of the *Re state in **Re124W** (left) and **Re126WW** (right) using spin-density distribution. The two situations differ mainly in the hole localization (blue) while the excited electron is in both cases localized at dmp (red). Typically, *Re is a combination of these two limiting situations. "Pure" ^{3}CT was not observed at any of the calculated trajectories.
Obtained by UKS calculation of the lowest triplet state at the PBE0-GD3BJ/6-31+G(d)/SDD level where interaction with the MM part was included at the level of electronic embedding. Structures were taken from specified TDDFT QM/MM/MD trajectories that are shown in Figs. 4, S7-8. Contours correspond to 0.002 a_0^{-3}.

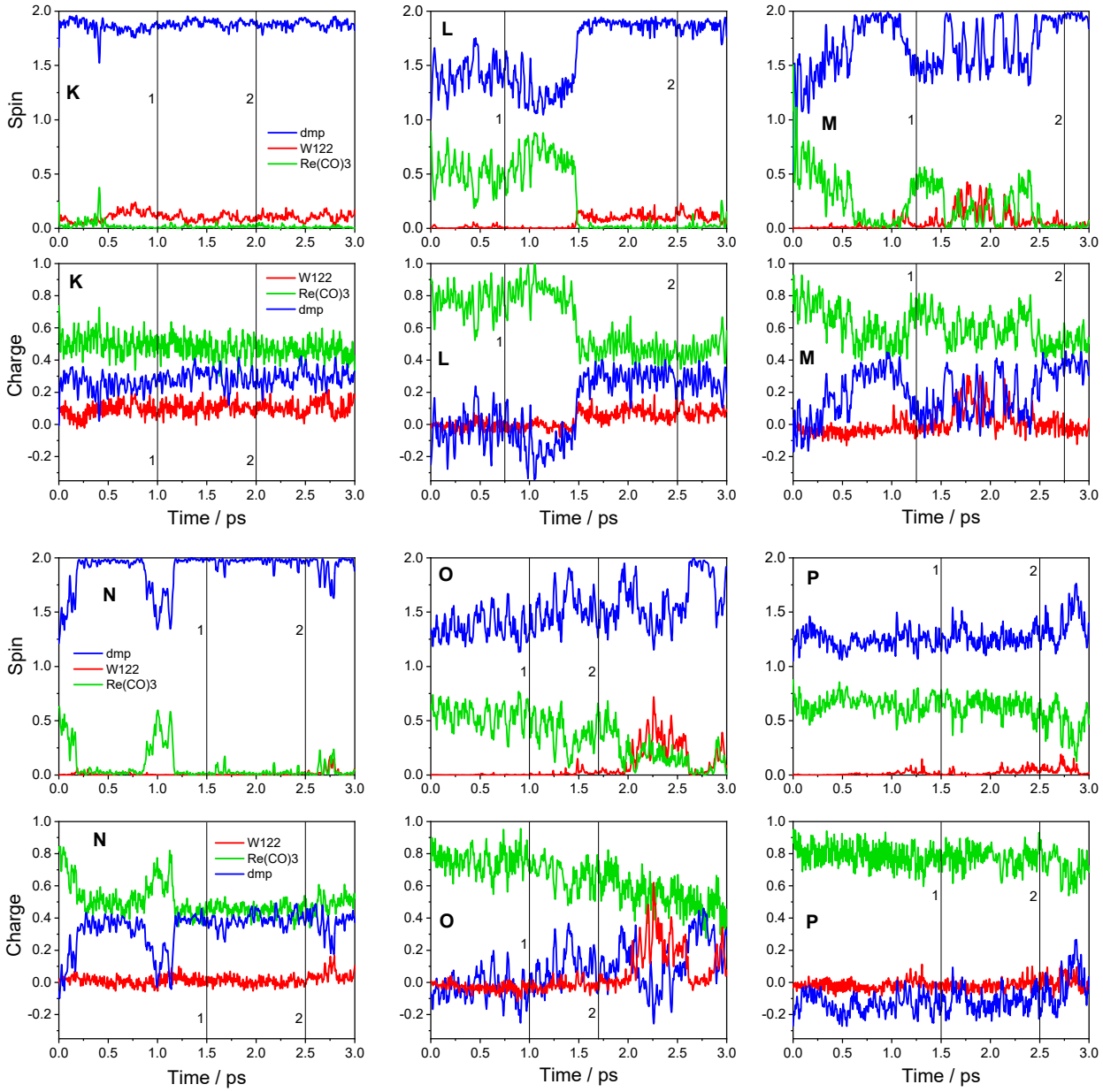

Fig. S5. UKS/MM/MD spin and charge trajectories of the lowest triplet excited state *Re of **Re124W** showing variable CT – IL mixing. Limiting ππ*(dmp) IL is described by spin 0 at Re and 2 at dmp; limiting CT by spin 1 at both dmp and $Re(CO)_3$. Note the regions (2.0-2.5 ps) of dmp–W122 delocalization on trajectories M and O. Numbered vertical lines denote starting times for TDDFT dynamics. Spin expressed as a difference between α- and β-spin electron populations. Charges obtained by Mulliken population analysis.

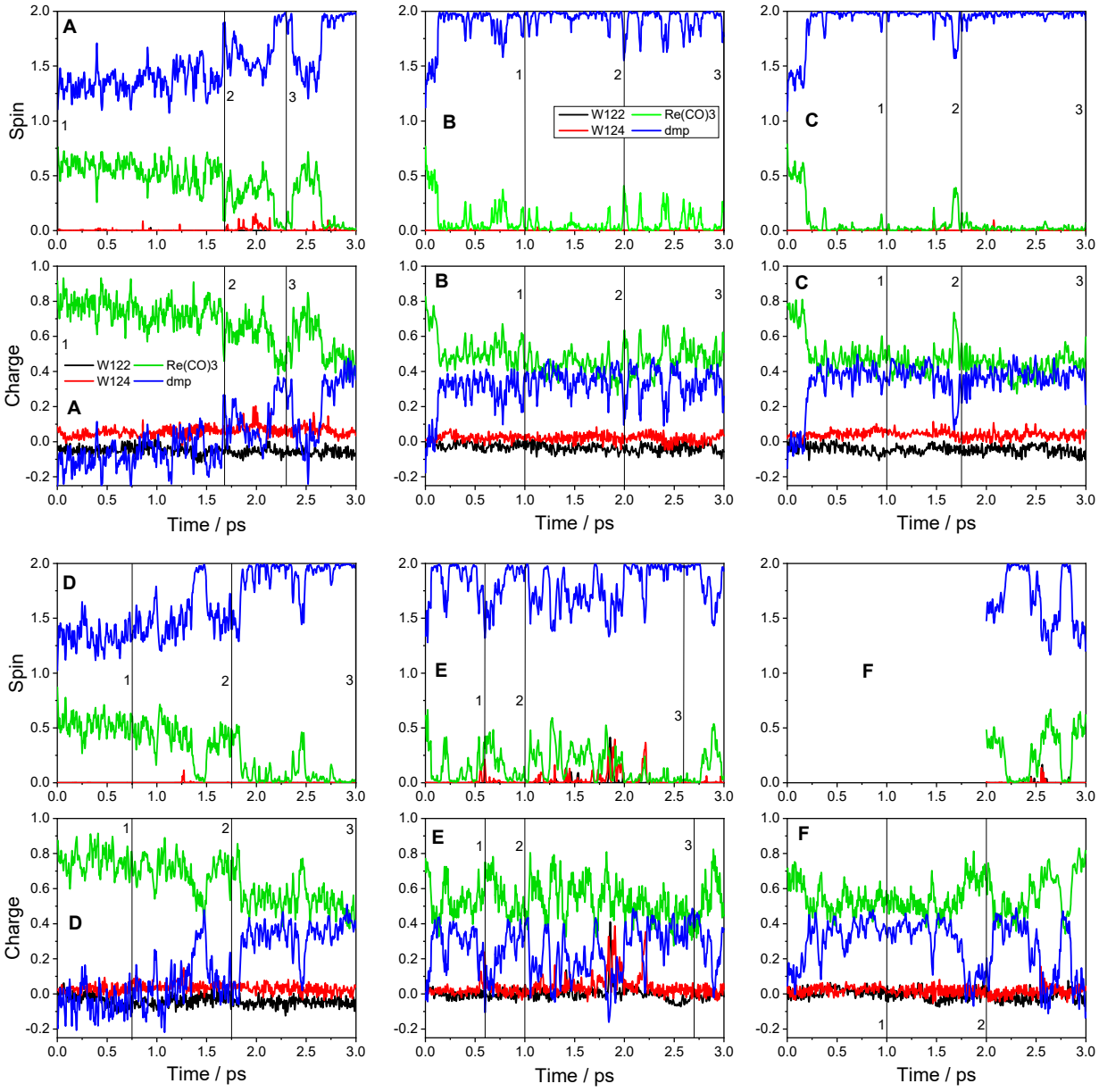

Fig. S6. UKS/MM/MD spin and charge trajectories of the lowest triplet excited state *Re of **Re126WW** showing variable CT – IL mixing. Limiting $\pi\pi^*$(dmp) IL is described by spin 0 at Re and 2 at dmp; limiting CT by spin 1 at both dmp and $Re(CO)_3$. Note the slightly more positive charge on W124 than W122 in most trajectories. Numbered vertical lines denote starting times for TDDFT dynamics. Spin expressed as a difference between α- and β-spin electron populations. Charges obtained by Mulliken population analysis.

S3. TDDFT QM/MM/MD trajectories

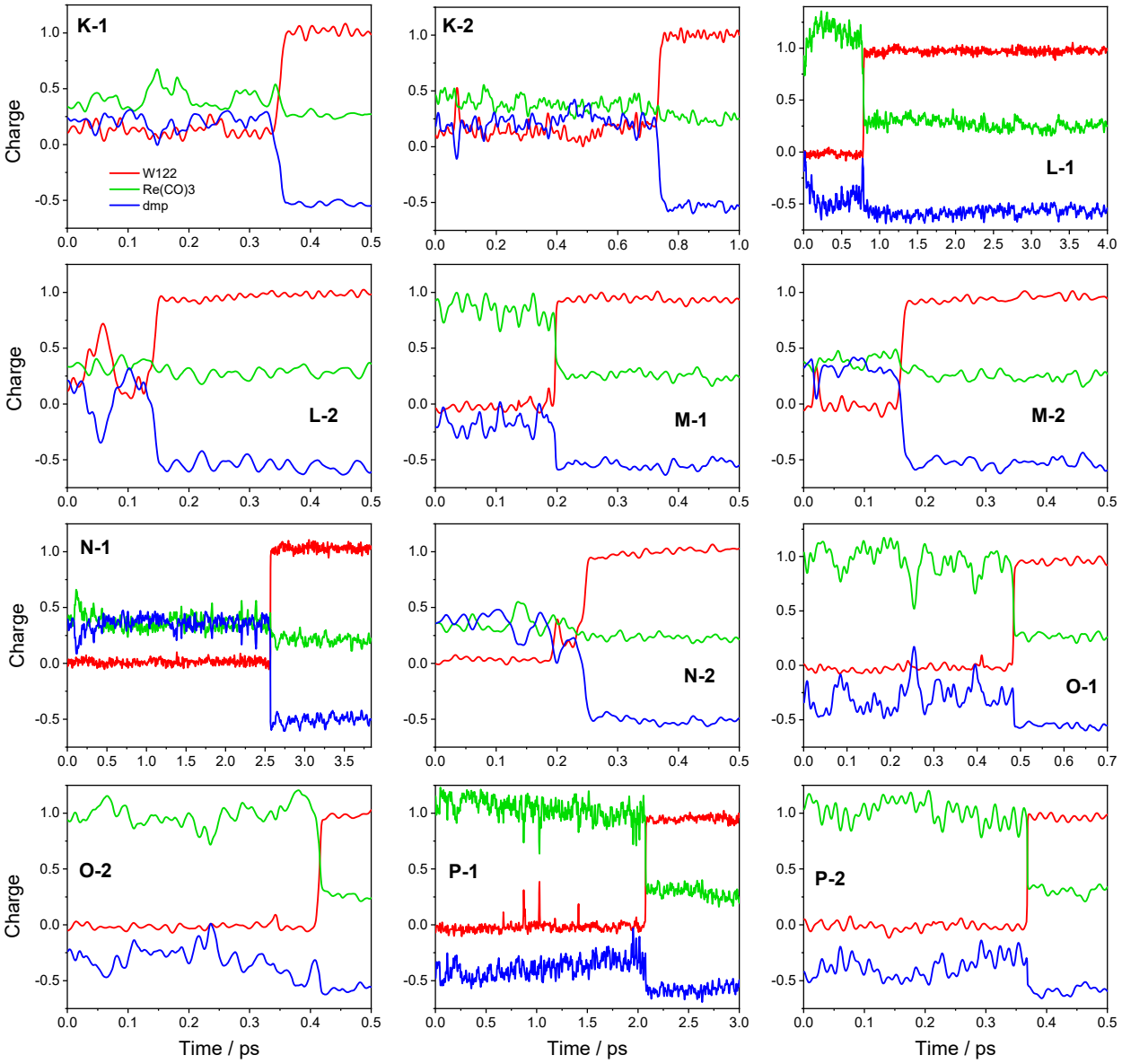

Fig. S7. Lowest triplet-state charge dynamics of **Re124W**. The panels X-# show TDDFT /MM/MD charge trajectories of the lowest excited triplet state calculated from starting points specified on the UKS trajectories (X = MM starting point; # = UKS starting point). Vertical jumps signify *Re/CS1 electronic-state crossings, *i.e*. electron transfer from W122 to *Re(CO)$_3$(dmp). Charges obtained by Mulliken population analysis.

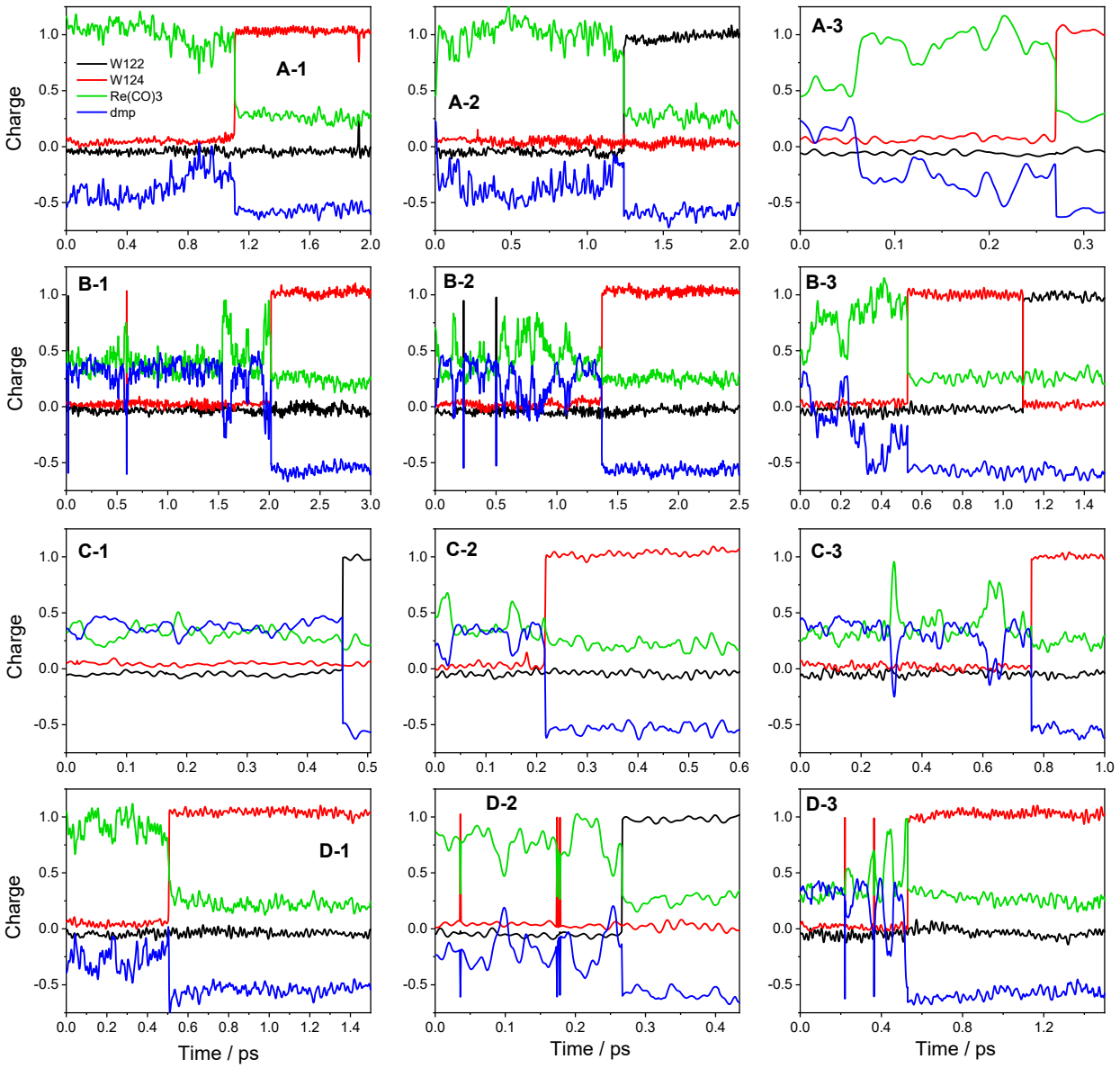

Fig. S8. Lowest triplet-state charge dynamics of **Re126WW.** The panels X-# show TDDFT/MM/MD charge trajectories of the lowest triplet excited state calculated from starting points specified on the UKS trajectories (X = MM starting point; # = UKS starting point). Red and black vertical jumps signify state crossings involving electron transfers from W124 and W122, respectively. (His126 and imidazole charge trajectories did not exhibit any significant fluctuations.) Charges obtained by Mulliken population analysis.

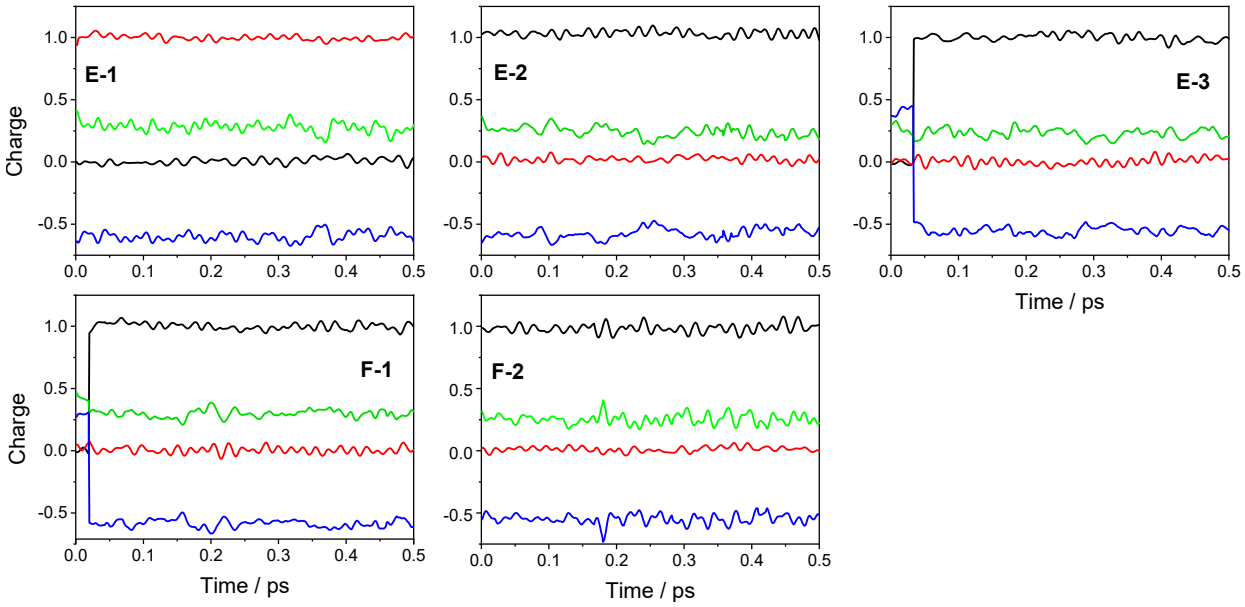

Fig. S8. continued. Note that F-1 and F-2 correspond to the "distant" conformation with the dmp ligand rotated away from W124.

S4. Examples of TDDFT energy trajectories (L-1 and A-3)

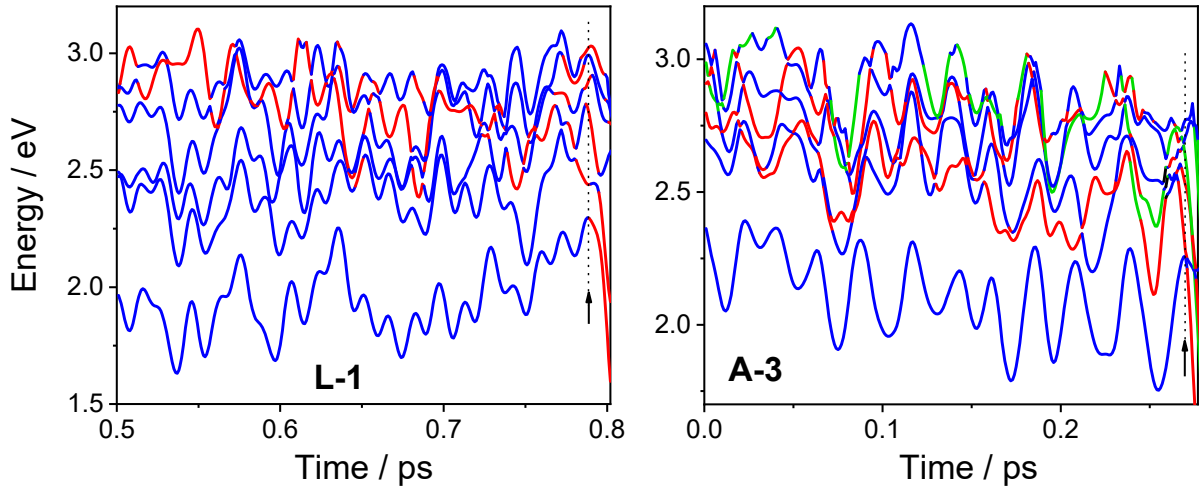

Fig. S9. TDDFT/MM/MD energy trajectories of six lowest triplet excited states of **Re124W** (L-1) and **Re126WW** (A-3) ~0.3 ps before the *Re/CS1 crossing. Blue: Re(H124/H126)$(CO)_3$(dmp) – localized *Re-type states defined by a total charge on the Re complex >0.5; Red: states with predominant CS1 character defined by total charge on the proximal indole >0.5. Green: states with predominant CS2 character defined by total charge on the **Re126WW** W122 indole >0.5. Arrows and dotted vertical lines denote crossing times.

S5. Effect of adding water molecules to the quantum space

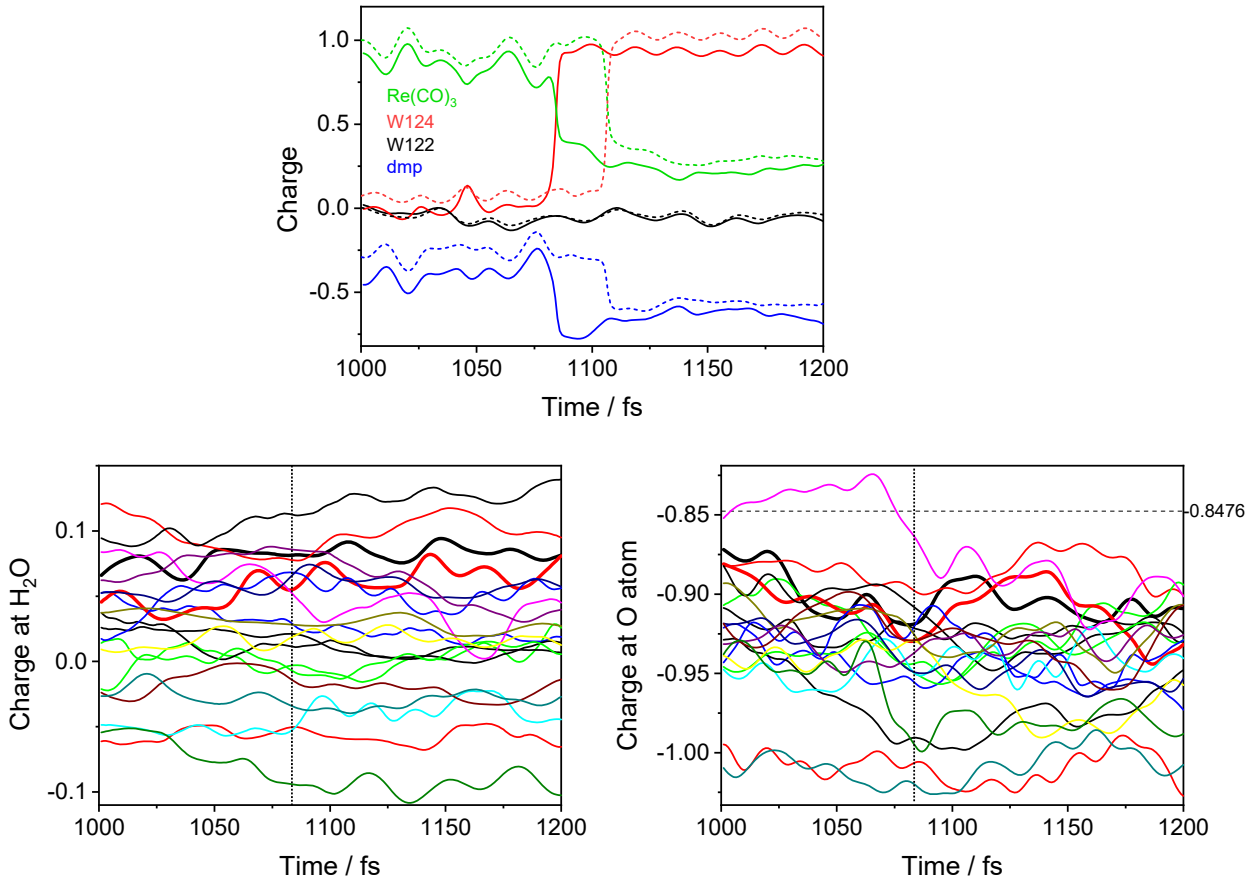

Fig. S10. Top: TDDFT QM/MM/MD charge trajectories A-1 (**Re126WW**) calculated with all water molecules treated classically by MM (dashed) and with 20 nearest water molecules included in the quantum space (full line).
Bottom-left: Trajectories of the total charge at each of the 20 H_2O molecules treated quantum mechanically. Black-bold: H_2O closest to the W124 N–H group. Red-bold: H_2O closest to the W122 N–H group. Dotted vertical line denotes the *Re/CS1 crossing time.
Bottom-right: Trajectories of the charge at the O atom of each of the 20 H_2O molecules treated quantum mechanically. Horizontal dashed line at -0.8476 e shows the partial charge of the oxygen atom of the SPC/E water model used together with the AMBER 14 force field. The figure indicates small polarization of the H_2O molecule next to W124 N–H (black bold) and, with a delay, of the H_2O molecule next to W122 N–H (red-bold).
All charges were obtained by Mulliken population analysis.

S6. Effects of changing the computational protocol on state crossing

Recalculation of the charge and spin distribution in the lowest excited state along the trajectories A-1, A-2, and B-3 by the UKS method reproduced the state crossings exhibited by the TDDFT originals (Fig. S11). The UKS B-3 trajectory exhibited extensive charge and spin delocalization between W124 and $W122^{\bullet+}$ in CS2, manifested by large anticorrelated oscillations after ~1.1 ps (Fig. S11c).

TDDFT trajectories calculated with the long-range corrected CAM-B3LYP functional instead of PBE0 did not show state crossings because all CS states were initially too high in energy. However, recalculating A-1 with CAM-B3LYP at PBE0-obtained geometries showed the *Re/CS1 crossing, although it was spread over a longer time interval and reversible (Fig. S12a). CAM-B3LYP recalculation of the A-1 region around 4 ps reproduced a stable CS1 state (Fig. S12b). CAM-B3LYP UKS A-1 trajectory (Fig. S12c) exhibited a change in the lowest triplet state character to CS1 at 1.012 ps, similarly to PBE0 (Fig. S11a). However, a gradual decrease (increase) of W124 (dmp) charges after 1.020 ps indicated either reversibility of the *Re/CS1 conversion or increasing delocalization. Recalculation of parts of B-3 and A-2 trajectories deep in the CS2 region (Fig. S12d,e) with CAM-B3LYP confirmed a stable $Re^{I}(CO)_3(dmp^{\bullet-})(W124)(W122^{\bullet+})$ charge distribution in the CS2 state, not indicating any charge delocalization between the two tryptophans.

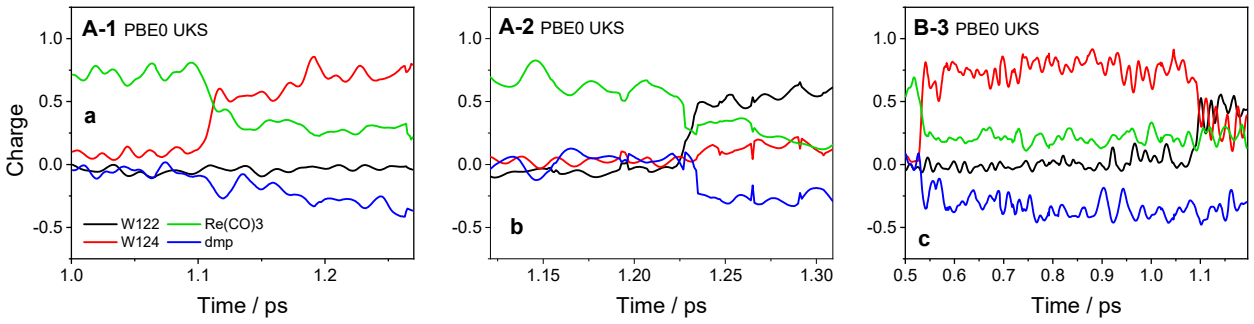

Fig. S11. UKS-calculated charge distribution in the lowest triplet excited state in the vicinity of state crossings on A-1 (a), A-2 (b), and B-3 (c) trajectories using the PBE0 functional at TDDFT obtained geometries. Charges obtained by Mulliken population analysis.

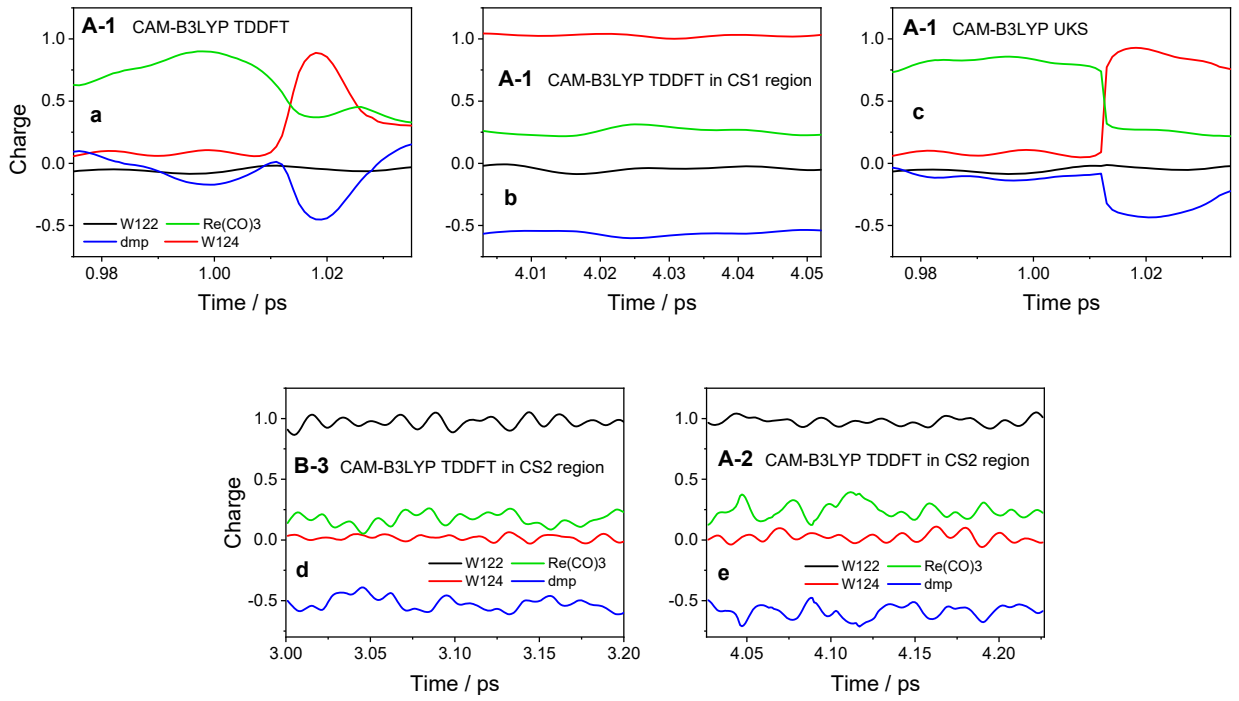

Fig. S12. Reruns of charge trajectories with the CAM-B3LYP functional. a: TDDFT QM/MM/MD calculation at PBE0-obtained A-1 geometries in the crossing region. b: TDDFT QM/MM/MD calculation in the CS1 region starting from the PBE0-obtained geometry at 4003 fs. c: UKS-calculated charge distribution in the lowest triplet state in the vicinity of the state crossing on the A-1 trajectory (this is a CAM-B3LYP counterpart of Fig. S11a). d and e: TDDFT QM/MM/MD calculation in the CS2 region starting from the PBE0-obtained geometries B-3 at 3000 fs (d) and A-2 at 4026 fs (e). Charges obtained by Mulliken population analysis.

S7. Electronic coupling between *Re and CS states along TDDFT QM/MM/MD trajectories

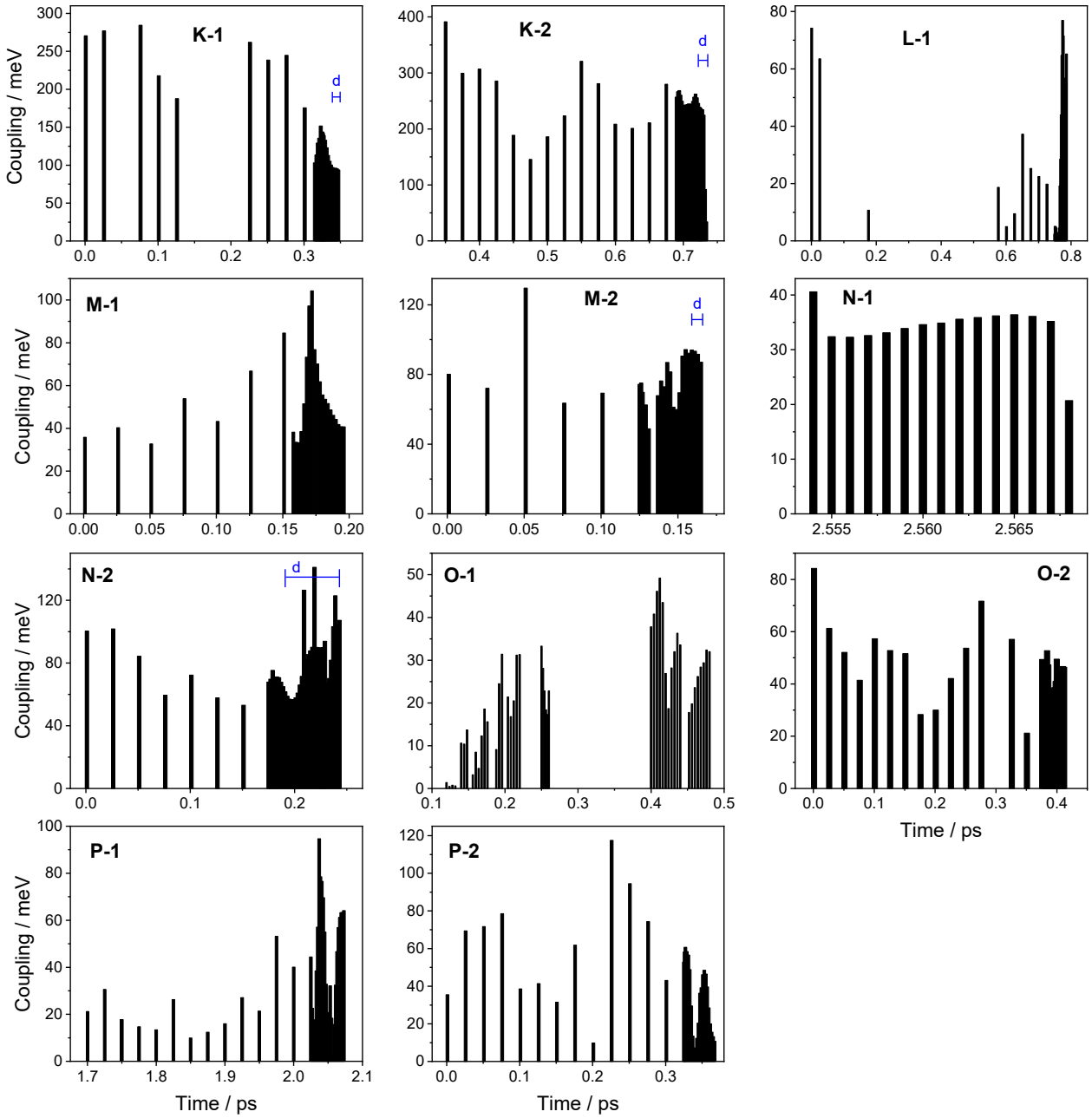

Fig. S13. Electronic coupling between the lowest *Re and CS1 states in **Re124W** calculated along TDDFT QM/MM/MD trajectories up to the state crossing; the last bar occurs approximately at the time corresponding to ~1/2 of the charge jump. Coupling values were calculated using the fragment charge differences approach (4-6). The blue segments denote time ranges of large delocalization of at least one of lower excited states over regions of the Re complex and the W122 indole.

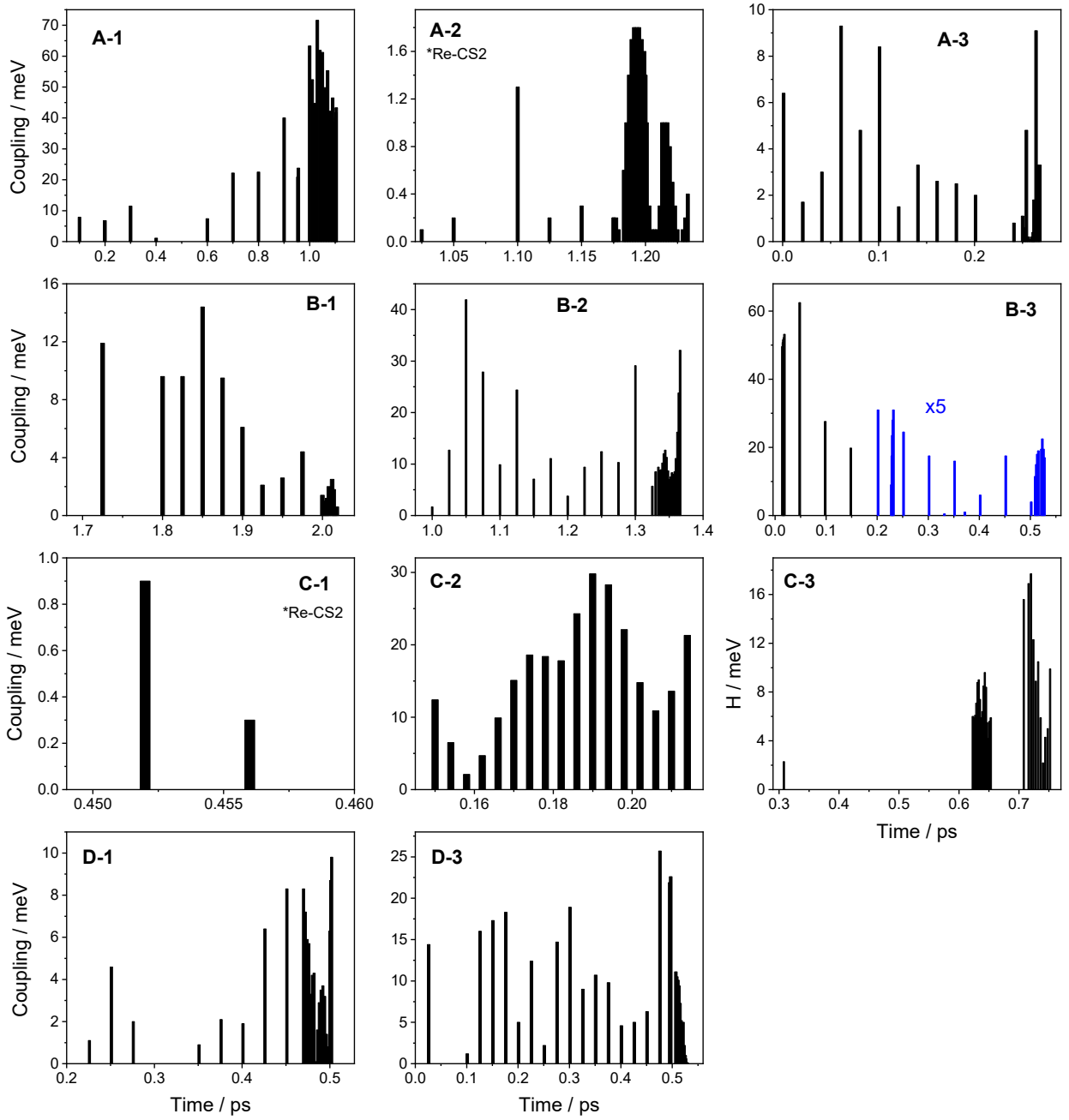

Fig. S14. Electronic coupling between the lowest *Re and CS1 states (CS2 on A-2 and C-1) in **Re126WW** calculated along TDDFT trajectories up to the state crossing; the last bar occurs approximately at the time corresponding to ~1/2 of the charge jump. (Trajectories calculated for the distant conformation F exhibited early direct *Re/CS2 crossings but the two states were essentially uncoupled: 0.0 (F-1), 0.1 meV (F-2).)

S8. Electronic coupling at state crossings, steric factors and molecular orbitals

Couplings calculated for **Re124W** and **Re126WW** at *Re/CS1 crossings are summarized in Tables S1 and S2 together with dmp–indole distances, angles and spatial overlaps. Mutual dmp–indole orientations are shown for typical cases in Figs. S15, S16. There is no single structural factor determining the coupling magnitude; and all factors must be considered together with the predominant *Re character discussed in the main text. The closest distance has only a small effect, probably owing to its small range and multiple dmp–indole interactions that need not be fully represented by the closest-distance value. Some trends are apparent when comparing trajectories of the same *Re character. For example, coupling decreases in the order M-2 > N-2 > N-1 as the closest aromatic C-C distance increases and all three cases are predominantly ^{3}IL. Also, the smallest calculated **Re124W** coupling at a crossing point (P-2) corresponds to a structure with the longest dmp–indole separation. Distance effects are even less obvious in **Re126WW**, probably because of a smaller range of values. Still, the strongest-coupled A-1 crossing occurs at the shortest distance between aromatic carbon atoms.

The angle between dmp and indole planes matters as well. The strongest coupling in **Re124W** occurs in slightly tilted configurations (~30°), although a nearly parallel N-2 (3.3°) is also relatively well coupled, probably owing to good spatial overlap between the aromatic rings (Fig. S15) and a short distance. Generally, the mutual orientation of the overlapping rings is more important that the absolute overlap magnitude. Two relative indole–dmp positions that result in strong coupling are demonstrated in Fig. S15 by the K-1 (similar to K-2) and M-2 cases. N-1 is an extreme case with minimal overlap but with a reasonable coupling that could be maintained through a dmp CH_3 group lying at a short distance just underneath the indole benzene ring (Fig. S14). Weakly coupled P-2 has a large spatial overlap of a different kind (similar to more strongly coupled P-1) whose effect is probably offset by a long C–C distance and prevailing CT character. Most strongly coupled **Re126WW** structures have the W124 indole T-positioned sideways to the dmp ligand and slightly tilted (~75°), whereas the two very weakly coupled outliers B-1 and D-3 exhibit nearly perpendicular T-orientation and the indole benzene ring pointing away from dmp (Fig. S16). In the B-1 case, the coupling decreases from ~10 to 0.6

meV along the trajectory and is accompanied by an increase of the indole-dmp angle from ~75 to almost 90°.

Tab. S1. *Re–CS1 coupling values, predominant *Re character and geometrical parameters calculated at crossing points of **Re124W** TDDFT QM/MM/MD trajectories.

Trajectory	*Re Character	Crossing time (fs)	Coupling (meV)	Angle[a] (deg)	Shortest (arom)[b] (Å)	Shortest[c] (Å)	Contact[d]	Overlap[e] (Å^2)
K-1	IL	339	97.0	27.0	3.10	2.41	M	1.28
K-2	IL	722	92.1	33.8	2.95	2.52	A	1.08
L-1	CT	784	54.7	33.8	3.15	2.04	M	1.40
M-1	IL/CT	196	40.7	35.9	3.30	2.61	M	2.88
M-2	IL	157	92.2	29.9	3.28	2.55	M	1.56
N-1	IL	118	35.2	27.7	3.67	2.51	M	0.08
N-2	IL	189	65.0	3.3	3.40	2.98	M	2.47
O-1	CT/IL	480	32.0	18.6	3.31	2.82	A	0.91
O-2	CT/IL	408	44.9	21.4	3.39	2.16	M	0.90
P-1	CT/IL	2071	63.3	23.3	3.34	2.58	M	3.30
P-2	CT	365	13.2	6.4	3.59	3.12	M	3.17

a: Angle between indole and dmp planes. b: Shortest distance between indole and dmp aromatic C atoms. c: The shortest dmp-indole distance. d: The dmp group involved in the shortest contact M = CH_3, A = aromatic C-H. e: Spatial overlap of indole and dmp projected to a common plane (see Fig. S14).

Tab. S2. *Re–CS1 coupling values, predominant *Re character and geometrical parameters calculated at crossing points of **Re126WW** TDDFT QM/MM/MD trajectories.

Trajectory	*Re Character	Crossing time (fs)	Coupling (meV)	Angle[a] (deg)	Shortest (arom)[b] (Å)	Shortest[c] (Å)	Contact[d]
A-1	IL/CT	1103	41.7	74.8	3.34	2.18	A
A-3	IL/CT	266	3.3	75.3	3.47	2.31	A
B-1	CT	2018	0.6	87.5	3.62	2.32	A
B-2	IL	1366	32.1	75.0	3.49	2.64	A
B-3	CT/IL	526	3.4	81.7	3.75	2.66	A
C-2	IL	210	13.6	68.8	3.81	2.49	M
C-3	IL	752	9.9	76.4	3.75	2.70	M
D-1	IL/CT	502	9.8	93.3	3.56	2.16	A
D-3	CT	529	0.1	87.2	3.72	2.30	A

a: Angle between indole and dmp planes. b: Shortest distance between indole and dmp aromatic C atoms. c: The shortest dmp-indole distance. d: The dmp group involved in the shortest contact M = CH_3, A = aromatic C-H.

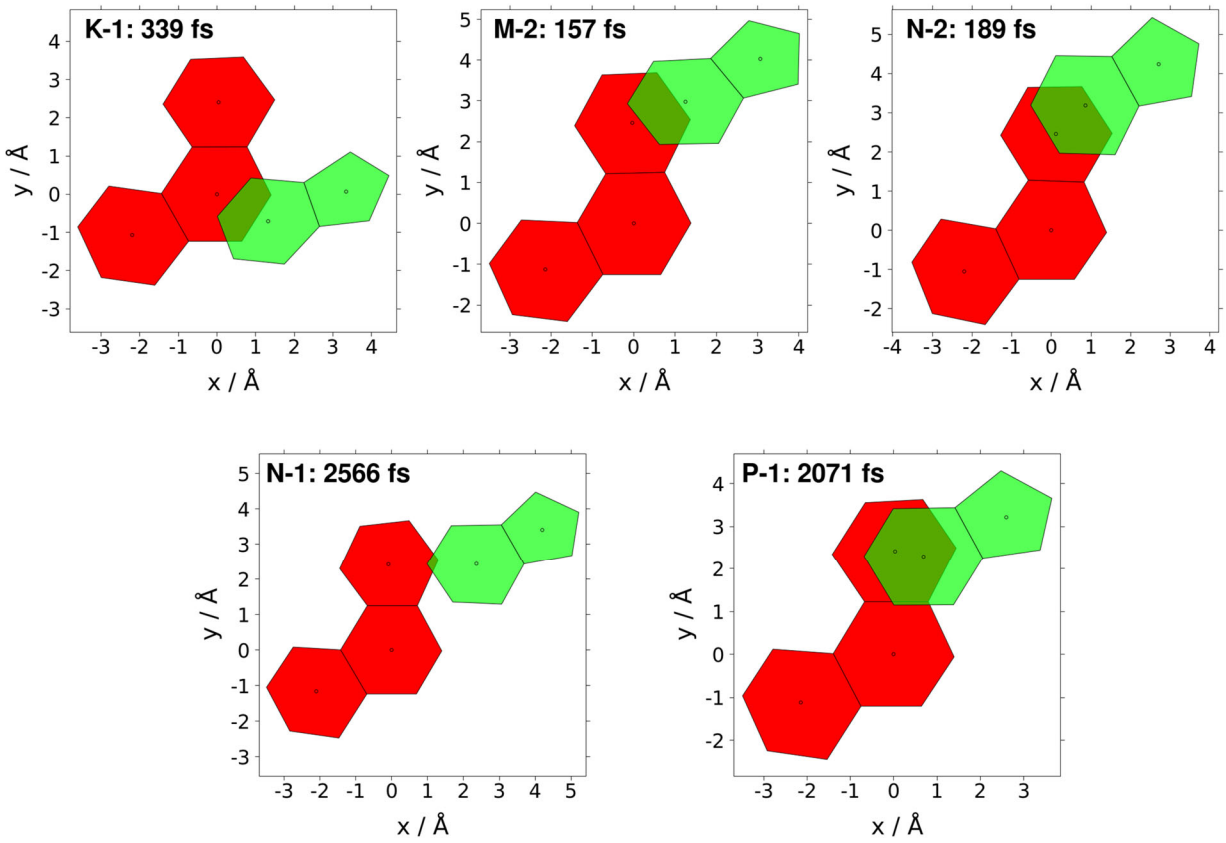

Fig. S15. Snapshots of **Re124W** trajectories at *Re/CS1 crossing: Projection of indole (green) and dmp (red) aromatic rings to a common plane. The trajectory and crossing time at which the snapshot was taken are shown in the top left corner of each panel. K-1 (97 meV, indole above the central C5-C6 bond) and M-2 (97 meV, indole above the C3-C4 bond) are examples of strongly coupled cases. Coupling at N-2 is weaker (65 meV) than at M-2 (92 meV) despite a larger overlap. N-1 has the smallest overlap of all calculated trajectories but still a reasonable coupling (35 meV), possibly due to interaction with a CH_3 group placed underneath the indole benzene ring. P-1 is weakly coupled (13 meV) despite a large overlap owing to predominant CT character of *Re and a large distance between the planes.

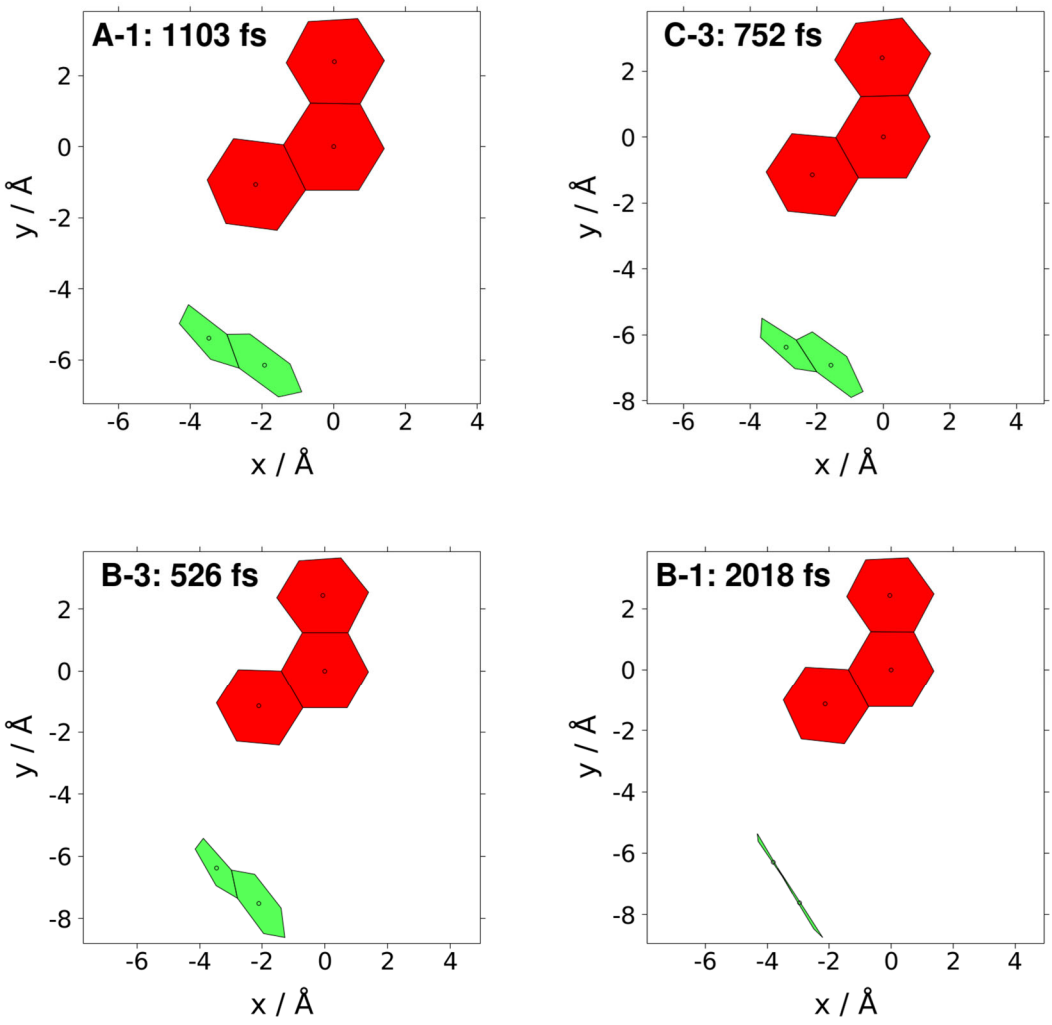

Fig. S16. Snapshots of **Re126WW** trajectories at *Re/CS1 crossing: Projections of indole (green) and dmp (red) aromatic rings to a common plane. The trajectory and crossing time at which the snapshot was taken are shown in the top left corner of each panel. A-1 and C-3 are examples of well-coupled cases (42 and 10 meV, resp.) where the indole is nearly aligned with the dmp C7-C8 bond. Coupling at B-3 is weaker (3 meV) despite a similar relative position, probably owing to the indole plane tilting away from the dmp C7-C8 bond. B-1 is very weakly coupled (0.6 meV), probably due to a large indole tilt away from dmp, nearly perpendicular orientation of their planes, and predominant CT character of *Re.

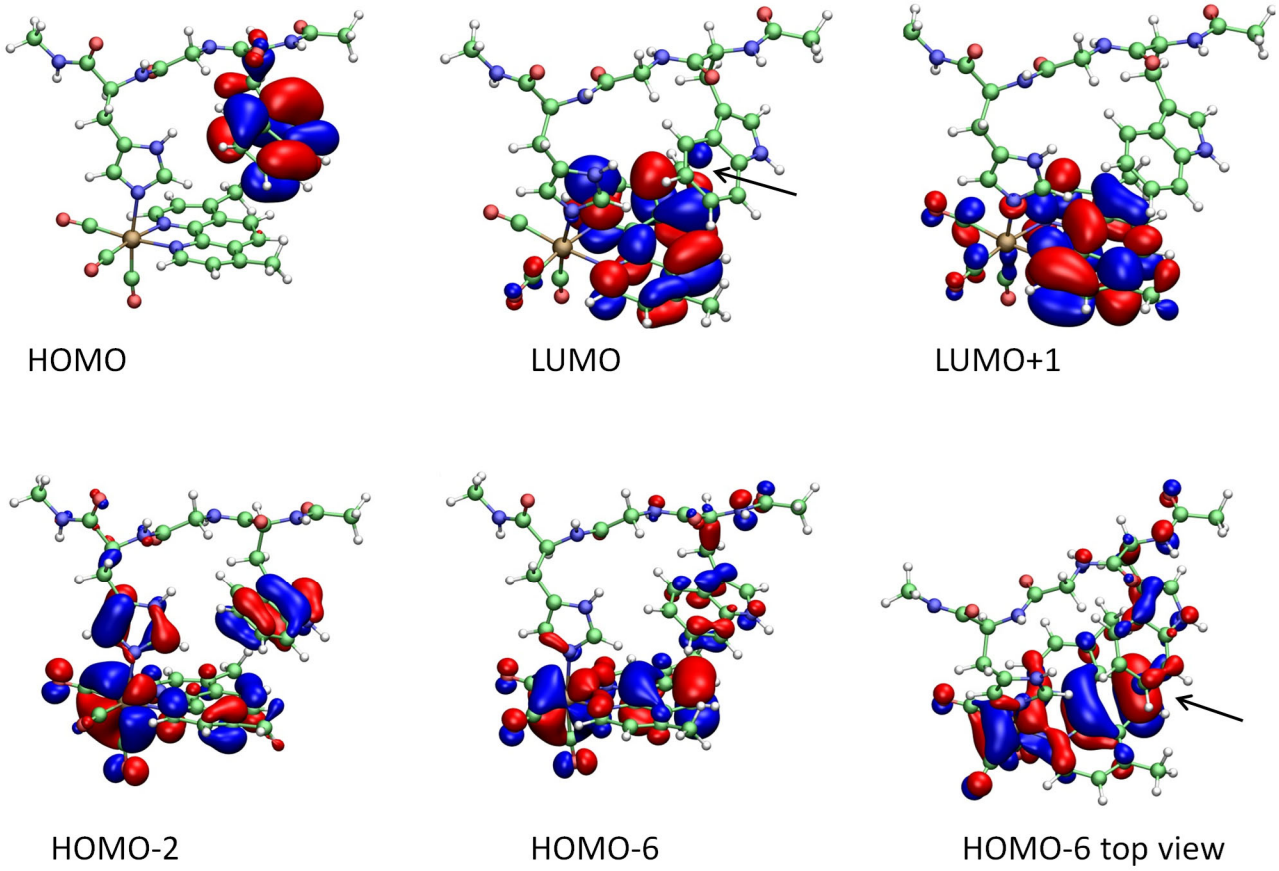

Fig. S17. Frontier molecular orbitals of **Re124W** important for *Re–CS1 coupling and *Re←W122 ET. Interactions of the indole-localized HOMO with LUMO, LUMO+1, HOMO-2 and HOMO-6 are expected to make important contributions. HOMO-2, and HOMO-6 are depopulated in the *Re state whose CT and IL components have large HOMO-2→LUMO, LUMO+1 and HOMO-6→LUMO contributions, respectively. The arrow in the LUMO picture indicates delocalization over the dmp CH_3 group lying underneath the indole. The HOMO-6 top view visualizes its delocalization over the indole (arrow). Calculated for K-1 at the crossing point (339 fs).

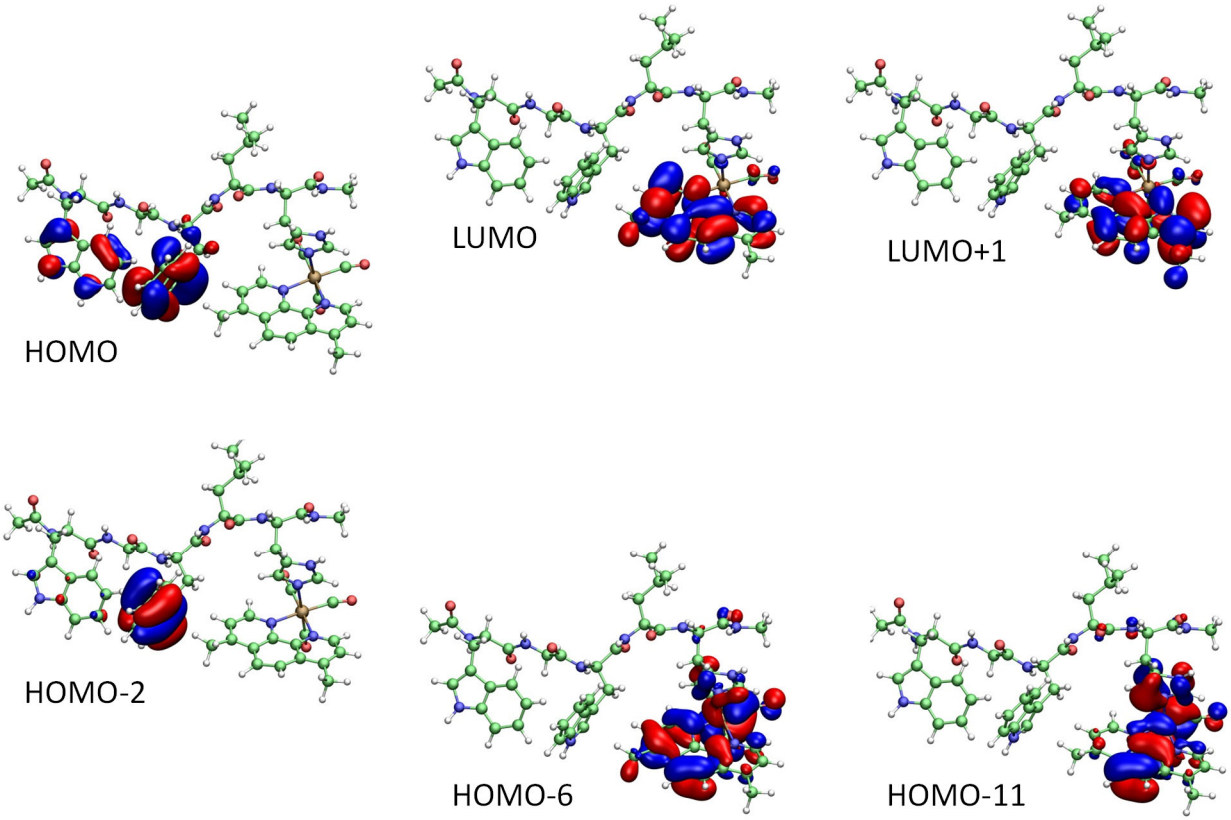

Fig. S18. Frontier molecular orbitals of **Re126WW** important for *Re–CS1 coupling and W124→*Re ET. (The Re complex is placed on the right-hand side.) Interactions of indole-localized HOMO and HOMO-2 (left column) with LUMO, LUMO+1, HOMO-6 and HOMO-11 are expected to make important contributions. HOMO-6 and HOMO-11 are depopulated in the *Re state whose CT and IL components have large HOMO-6→LUMO, LUMO+1 and HOMO-11→LUMO contributions, respectively. HOMO-6, and HOMO-11 are delocalized over the whole Re complex, blurring the distinction between CT and IL one-electron excitations. Calculated for C-3 at the crossing point (752 fs).

S9. Solvation: definitions of proximal volumes, distribution functions, and distances among W122-indole, A119 oxygen, and water molecules

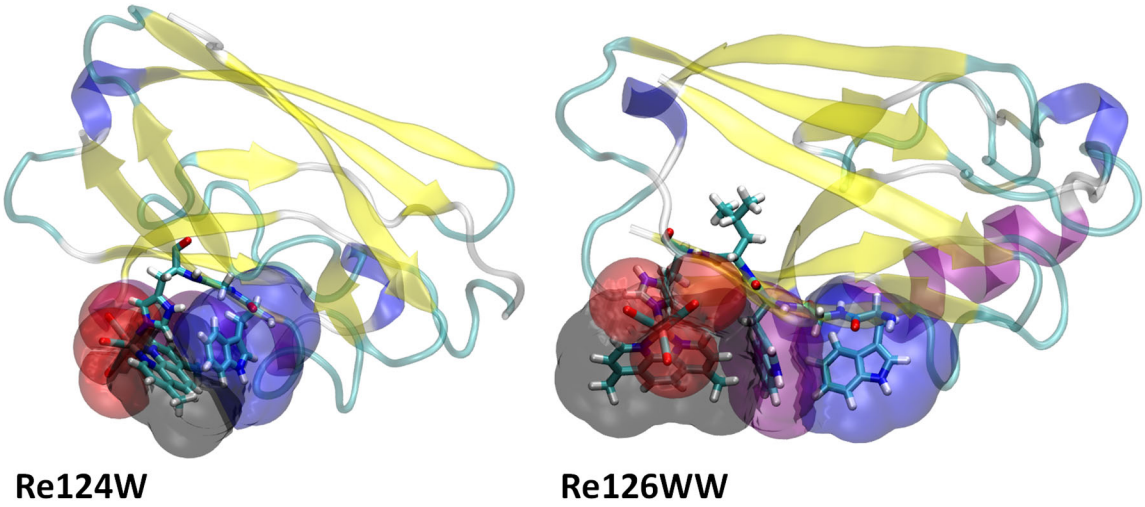

Fig. S19. Non-overlapping proximal volume shells around individual fragments used to calculate water proximal radial distribution functions g(*r*) (7). Blue: W122, violet: W124, gray: dmp, red: $(CO)_3$.

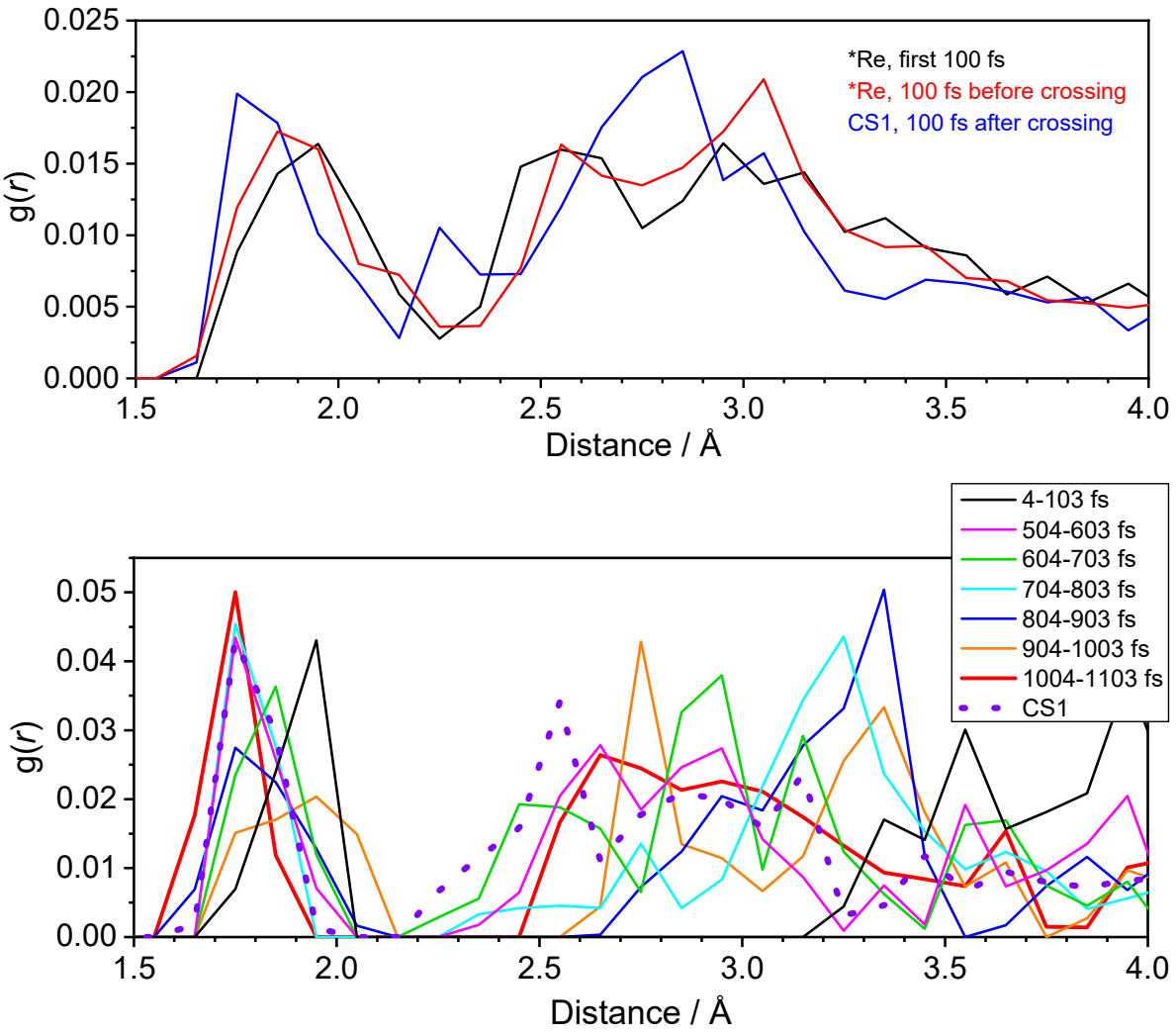

Fig. S20. Time-evolution of g(*r*) around W124 indole in **Re126WW**.
Top: g(*r*) averaged over TDDFT/MM/MD trajectories showing *Re/CS1 crossing during first 100 fs of each trajectory (black), last 100 fs before the crossing (red), and first 100 fs after the crossing – in the CS1 region.
Bottom: g(*r*) calculated over 100-fs intervals of the trajectory A-1 shown as solid lines. Bold-red: the last interval before the crossing. Dotted/bold-violet g(*r*) calculated over the whole CS1 region after the crossing. The figure shows that g(*r*) in the 1.5 – 2.2 Å evolves in the direction of the CS1 product while fluctuating back and forth.

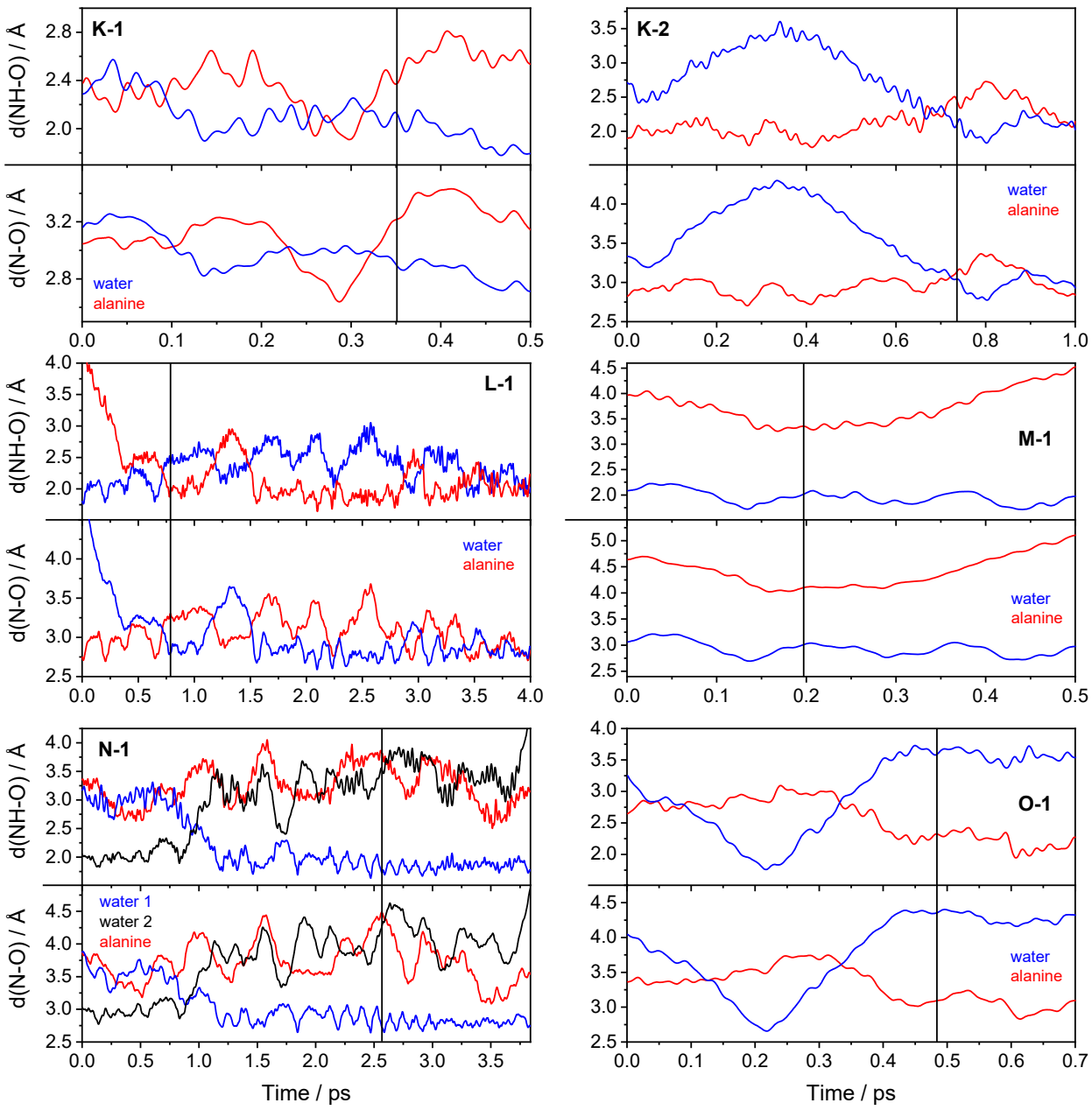

Fig. S21. Time-evolution of shortest W122-indole – water (blue, black) distances and of the W122-indole – O(A119) (red) distance along typical TDDFT trajectories of ***Re124W**. Top panels: NH–O distances, bottom panels: N–O distances. Vertical black lines mark times of *Re/CS1 crossings that occur mainly in situations where a water molecule lies closer than O(A119) or where both O atoms lie close, except for trajectories O-1 and O-2 where O(A119) is the closest.

Angles:

Average N–H–O(A119) angles over individual **Re124W** trajectories are: 129° (K-1), 139° (K-2), 129° (L-1), 128° (M-1), 127° (M-2), 111° (N-1), 109° (N-2), 131° (O-1), 142° (O-2), 107° (P-1), 106° (P-2).

Average N–H–O(nearest H_2O) angles: 143° (K-1), 140° (K-2), 138° (L-1), 164° (M-1), 159° (M-2), 146° (N-1), 143° (N-2), 139° (O-1), 130° (O-2), 156° (P-1), 156° (P-2). The closest water molecule lies nearly in the indole plane.

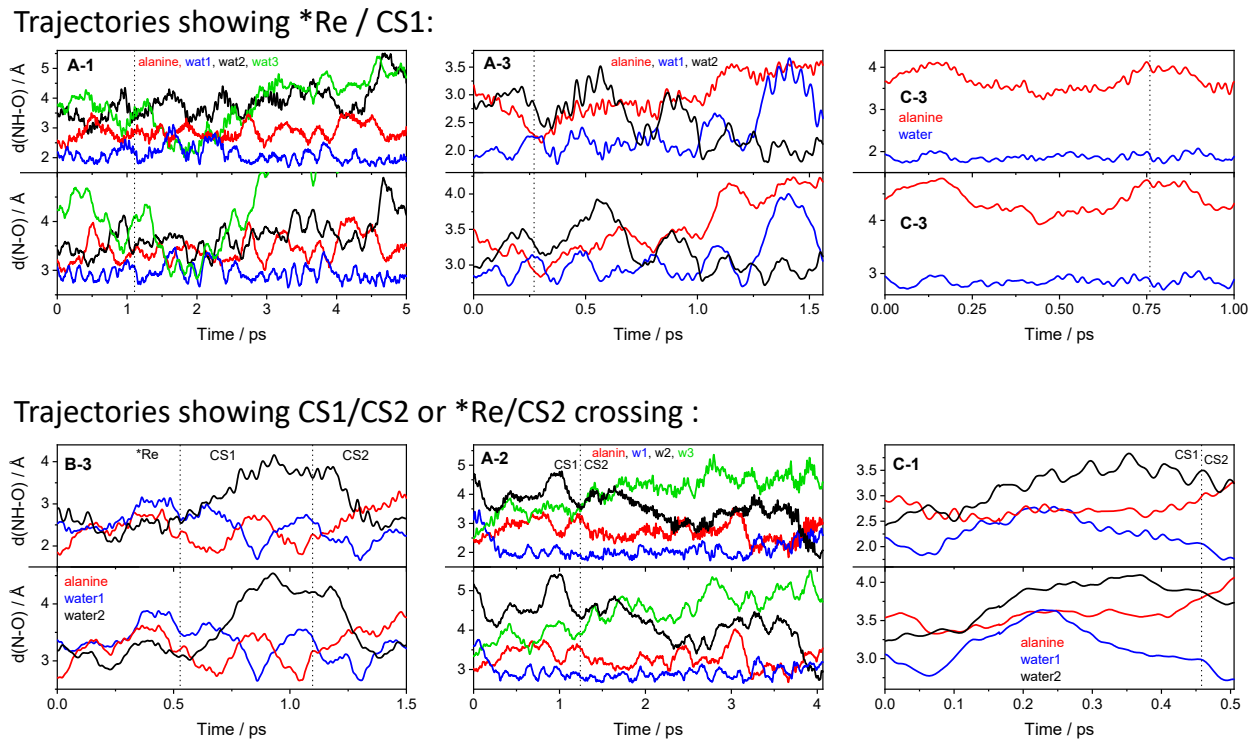

Fig. S22. Time-evolution of shortest W122-indole – water distances (blue, black, green) and of the W122-indole – O(A119) (red) distances along typical TDDFT trajectories of ***Re126WW**. Top panels: NH–O distance, bottom panels: N–O distances. Vertical black dotted lines mark times of electronic state crossing.

Upper row: Trajectories showing only *Re/CS1 crossing. W122 indole is solvated by 1-3 water molecules. Most of the time, the A119 O is the second closest oxygen atom to the indole NH, usually within H-bonding distance. Both A119 and nearest-H_2O oxygen atoms lie close to the indole plane: the angle between the indole plane and the line connecting the N and O atom (A119 or H_2O) usually lies within 20° and 30°, respectively.

Lower row: Trajectories showing sequential *Re/CS1 and CS1/CS2 crossings (B-3) or direct *Re/CS2 crossing (A-2, C-1). Most of the time, A119 O is the second closest oxygen atom to the indole NH, usually within H-bonding distance. The CS1/CS2 crossing at B-3 occurs in a situation where the alanine oxygen is closer to the indole NH but shortly before its replacement by a water oxygen atom. Both indole and nearby water O atoms lie close to the indole plane at the time of crossing (8° and 20°, resp.) and the N–H–O angles are 147° (A119) and 139° (nearest H_2O). The *Re/CS2 crossing at A-2 and C-1 occurs when the indole is primarily water-solvated but alanine and second-nearest water oxygen atoms are at comparable distances and close to the indole plane. At the A-2 trajectory, the N–H–O angles are 110° (A119) and 147° (nearest H_2O). At C-2, the N–H–O angles are 138° (A119) and 152° (nearest H_2O).

Average N–H–O(A119) angles for the investigated **Re126WW** trajectories: 116° (A-1), 114° (A-2), 116° (A-3), 139° (B-3), 141° (C-1), 129° (C-3). Average N–H–O(nearest H_2O) angles: 143° (A-1), 140° (A-2), 134° (A-3), 144° (B-3), 145° (C-1), 167° (C-3).

S10. Electrostatic potentials

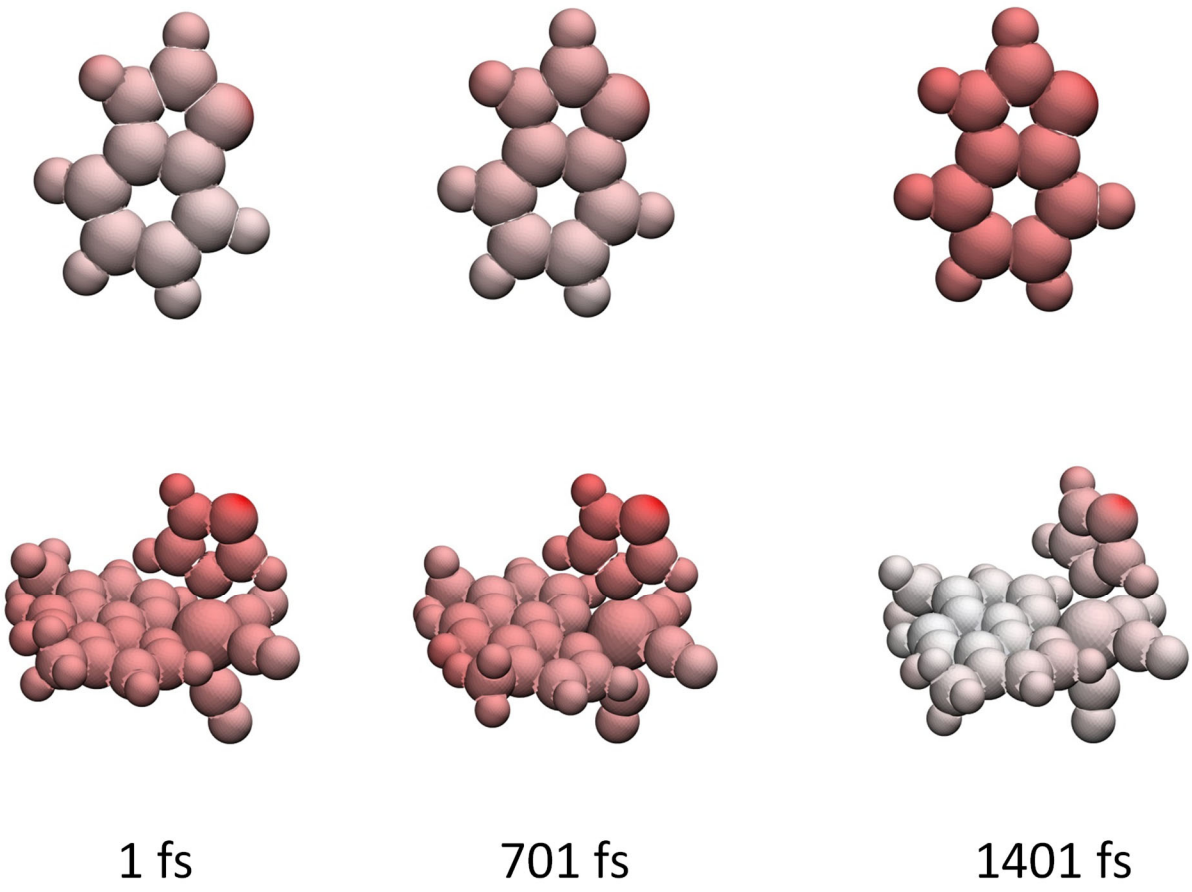

Fig. S23. Visualization of total electrostatic potential φ_{tot} generated by all surrounding atoms at the van der Waals surface of the W122 indole (top) and the Re(imidazole)$(CO)_3$(dmp)$^+$ complex (bottom) in **Re124W** calculated at the beginning of the L-1 trajectory (left), before (middle) and after (right) the *Re/CS1 crossing. Color shading/scaling in the range ±10.9 V; from red color for the negative bound through white for the zero potential to blue for the positive bound.

To obtain the potential distribution, van der Waals envelopes of a given molecular fragment were covered with triangles and the potential was calculated in their centers. φ-values characterizing the whole fragment and used in φ-trajectories (Fig. 6, etc.) were calculated as averages of center values weighted by triangle areas. φ_{tot}, φ_{MM}, and φ_{H2O} differ only in the origin of the electrostatic potential: all atoms of the system, all atoms of the MM part (water, the rest of the protein, and charge-compensating Na^+ ions), and all H_2O molecules, respectively.

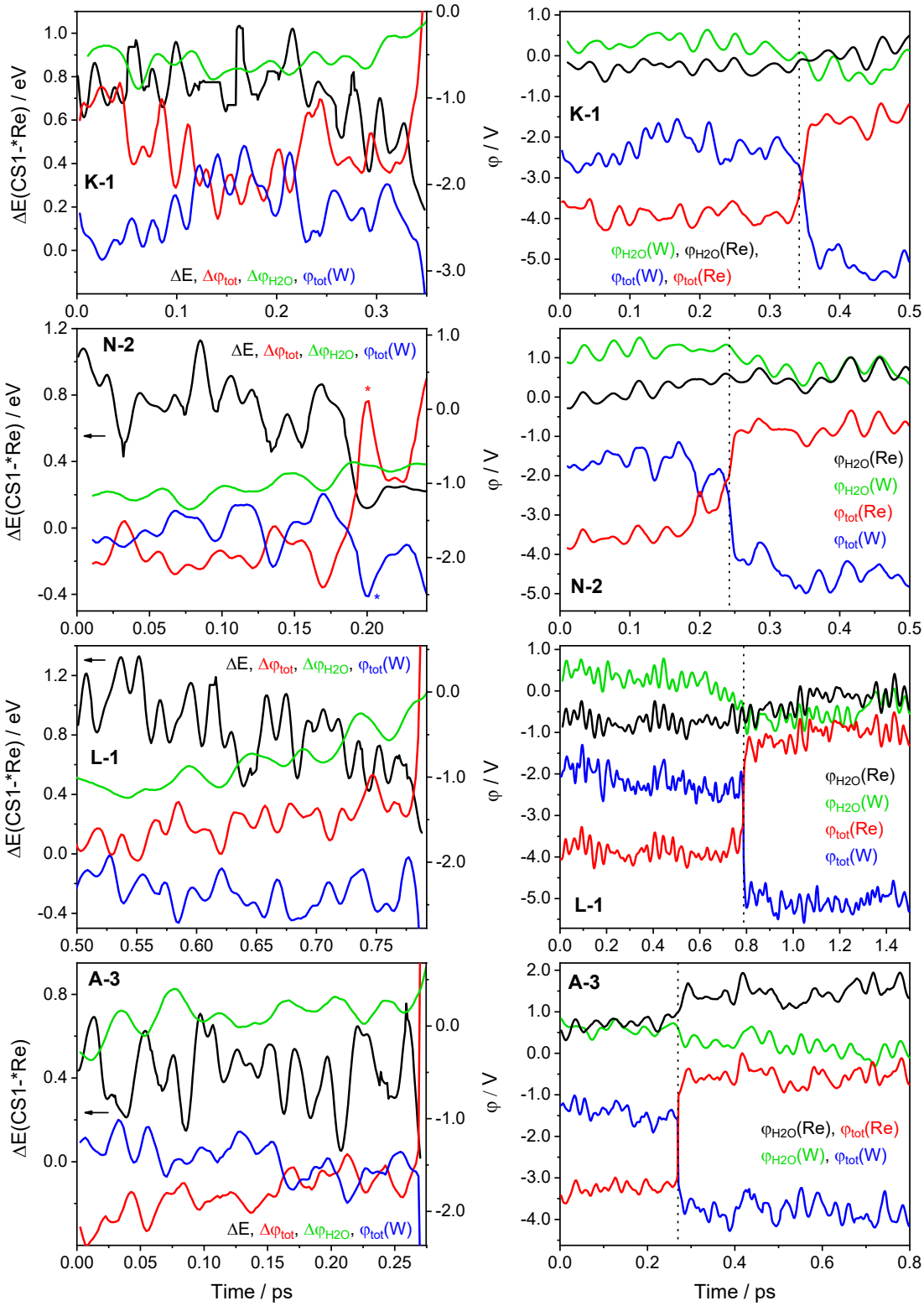

Fig. S24. Left: Time evolution of CS1–*Re energy difference (black, ΔE, left axis), difference $\Delta\varphi = \varphi(\mathrm{Re}) - \varphi(\mathrm{W})$ ($\Delta\varphi_{tot}$ red; $\Delta\varphi_{H2O}$ green), and of $\varphi_{tot}(W)$ (blue) along trajectories K-1, N-2, L-1, and A-3 up to the *Re/CS1 crossing. Right: Trajectories of φ_{tot} and φ_{H2O} at the Re complex and the proximal indole (W) before and after *Re/CS1 crossing marked by vertical dotted lines.

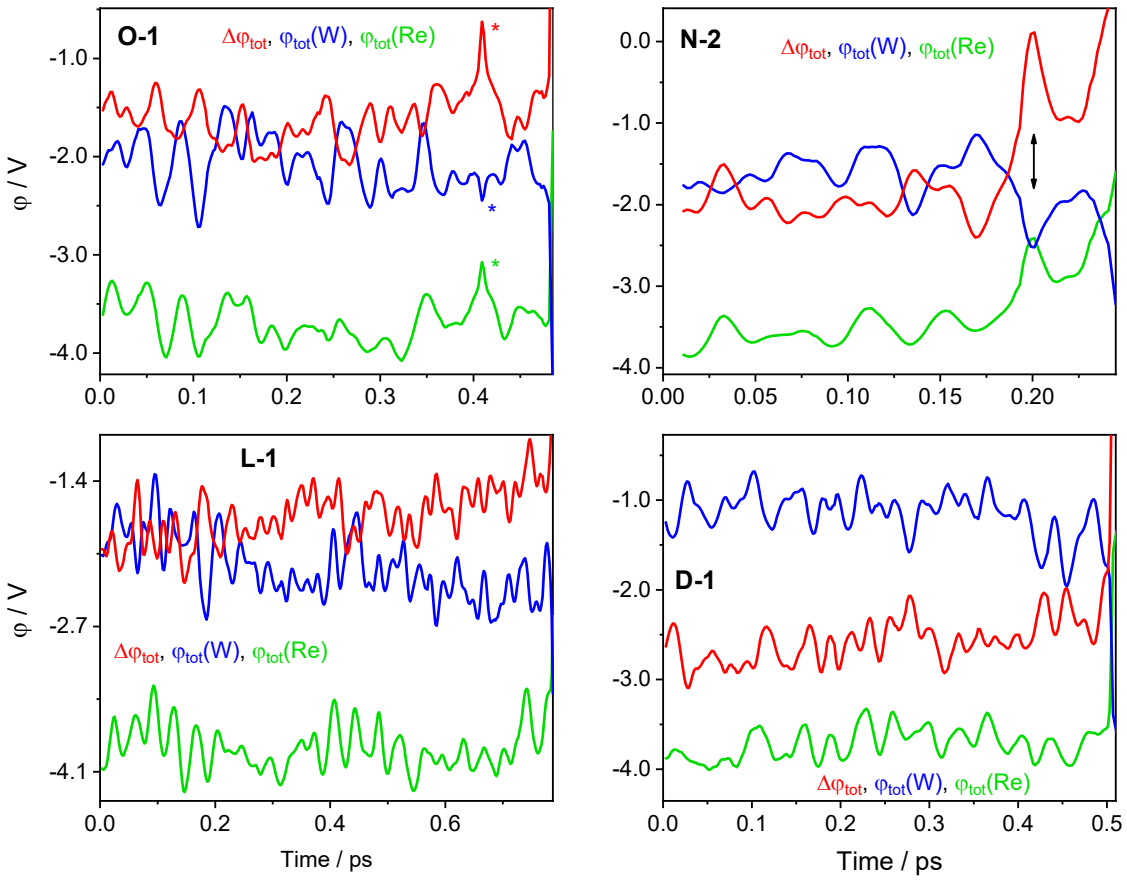

Fig. S25. Time evolution of $\Delta\varphi_{tot} = \varphi_{tot}(Re) - \varphi_{tot}(W)$ (red), $\varphi_{tot}(Re)$ (green) and $\varphi_{tot}(W)$ (blue, W = proximal indole). Features marked * (O-1) and double arrow (N-2) result from charge fluctuations between the *Re(His)$(CO)_3$(dmp) complex and W122 and reflect interactions between components of the QM part of the system. They are not visible on φ_{H2O} and φ_{MM} trajectories.

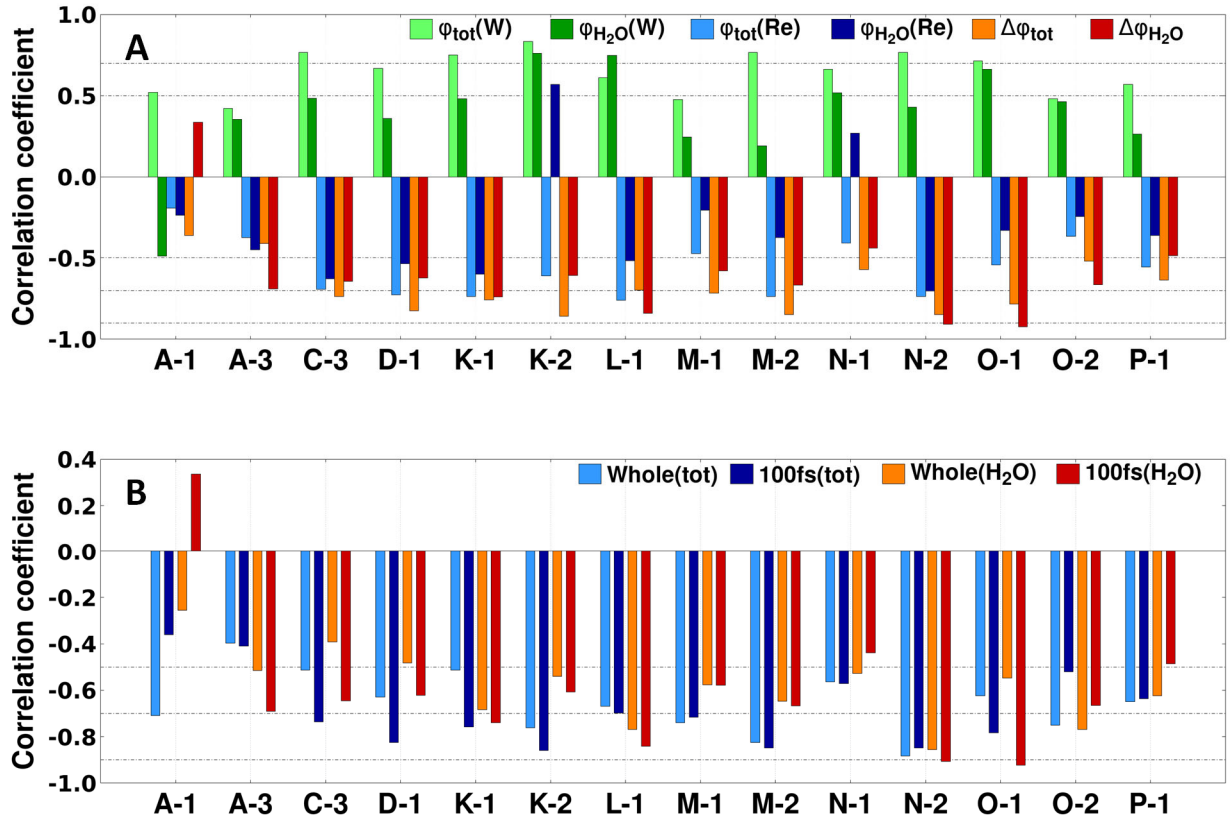

Fig. S26. Correlation coefficients between time evolutions of ΔE and $\Delta\varphi = \varphi(Re) - \varphi(W)$, $\varphi(Re)$, and $\varphi(W)$ calculated for individual trajectories. A: correlation coefficients calculated for φ_{tot} and φ_{H2O} over 100 fs before *Re/CS1 crossing. Positive and negative values mean correlation and anticorrelation, respectively. B: Comparison of ΔE–$\Delta\varphi_{tot}$ and ΔE–$\Delta\varphi_{H2O}$ correlation coefficients calculated over whole trajectories and over the last 100 fs before the *Re/CS1 crossing.

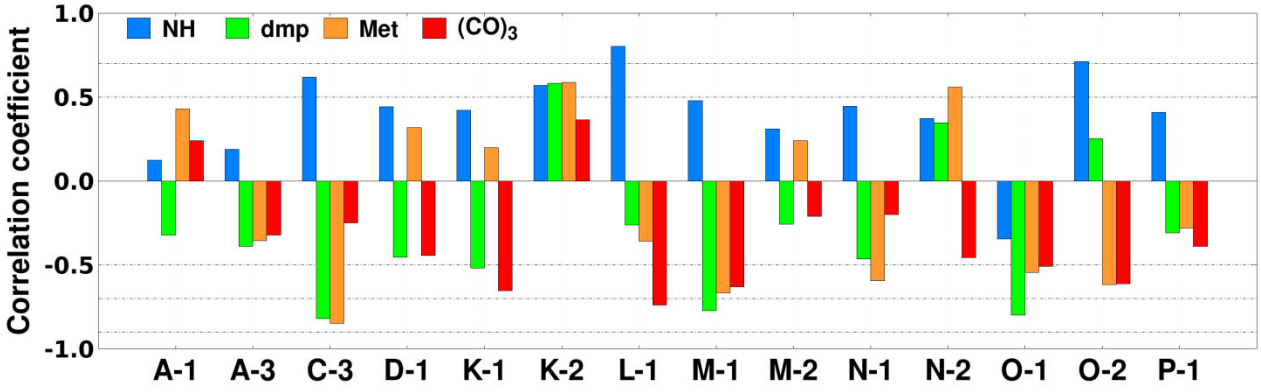

Fig. S27. Correlation coefficients between ΔE and φ_{H2O} at molecular fragments: NH of the proximal indole, dmp ligand, Me groups, and $(CO)_3$.

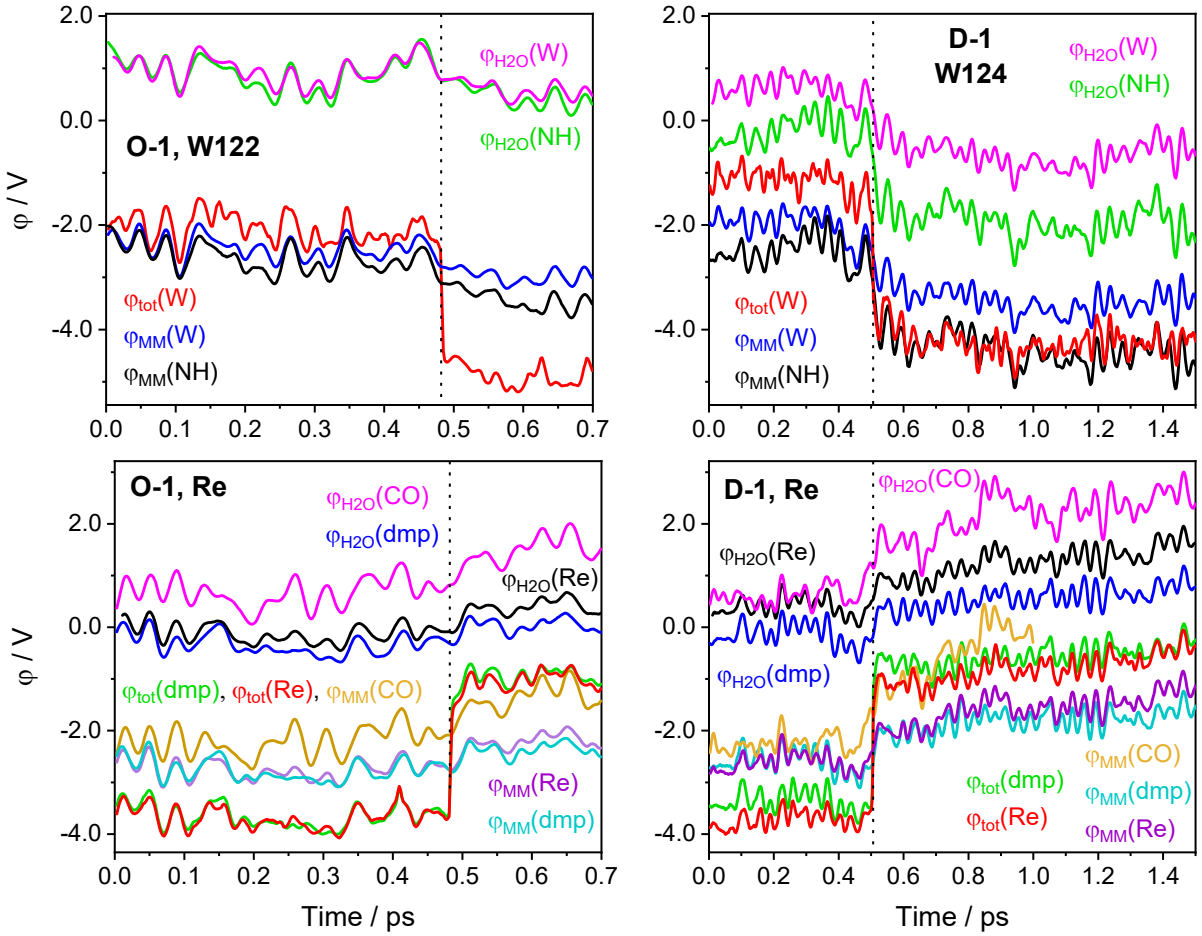

Fig. S28. **Re124W** O-1 (left) and **Re126WW** D-1 (right) trajectories of φ at the proximal indole (top) and the Re complex (bottom), together with φ at their molecular fragments NH, $(CO)_3$, and dmp. Potentials generated by all atoms (φ_{tot}), H_2O molecules (φ_{H2O}), and by all classically treated atoms (φ_{MM}) are compared.

The crossing region aside, time evolution of φ_{tot}(Re) is mostly driven by water fluctuations around the three CO ligands. This is demonstrated in the bottom panels, where Re, dmp, as well as CO φ trajectories largely follow φ_{H2O}(CO) that exhibits the largest fluctuation amplitudes. Similarly, indole-related trajectories essentially follow φ_{H2O}(NH) (top panels). Finer features and oscillations occasionally observable at φ_{tot}(Re) and φ_{tot}(W) trajectories arose from intramolecular vibrations and transient *Re–indole charge delocalization. (Features at ~400 fs (O-1) and ~200 fs (N-2) are cases in point (Fig. S25), where corresponding TDDFT charge trajectories exhibited short periods of W122–dmp delocalization.)

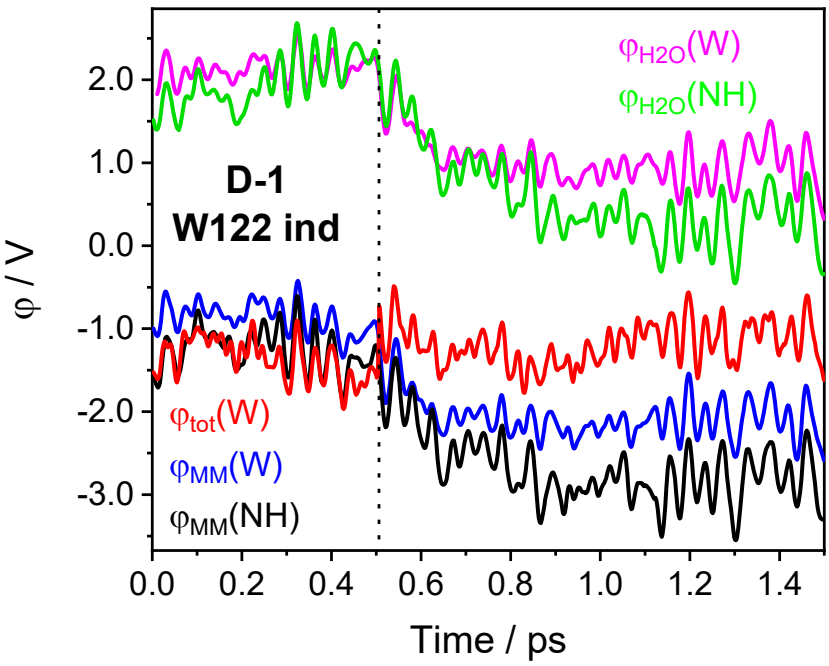

Fig. S29. Re126WW D-1 trajectories of φ_{tot}, φ_{H2O}, and φ_{MM} at the W122 indole and its NH fragment.

S11. Second electron "hop" in Re126WW (W124$^{\bullet+}$←W122)

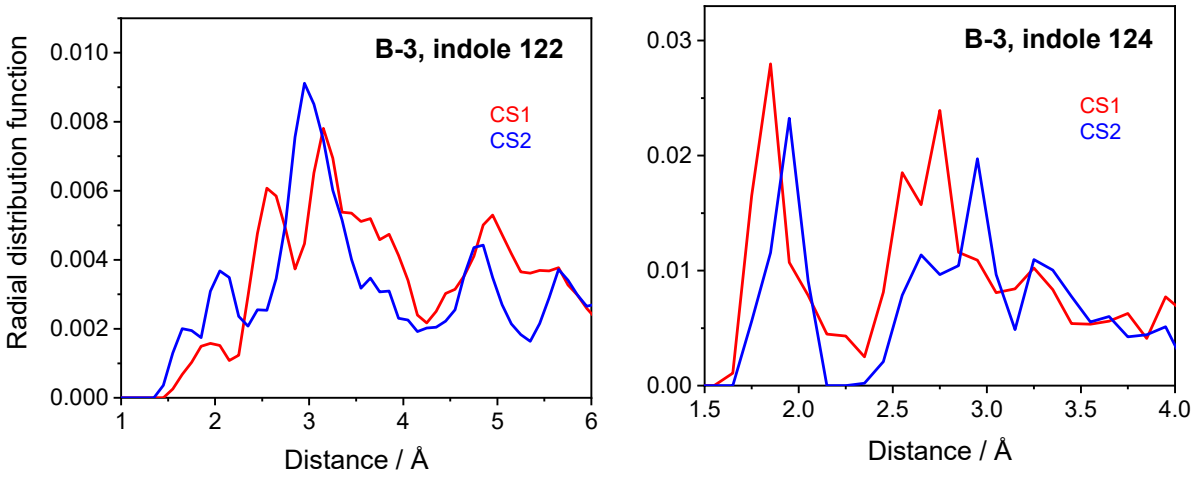

Fig. S30. Water proximal radial distribution function g(*r*) around W122 (left) and W124 (right) indoles in the **Re126WW** trajectory B-3 averaged over the CS1 region (red, 529–1097 fs) and the CS2 region (blue, 1098–1500 fs, 3-point adjacent averaging applied to W122 data).

Overall, g(*r*) changes around W122 indicate an increase in solvation and a shift of both solvation layers closer to W122 on going to CS2. Additional water molecules come from the vicinity of W124, where g(*r*) decreases and shifts farther.

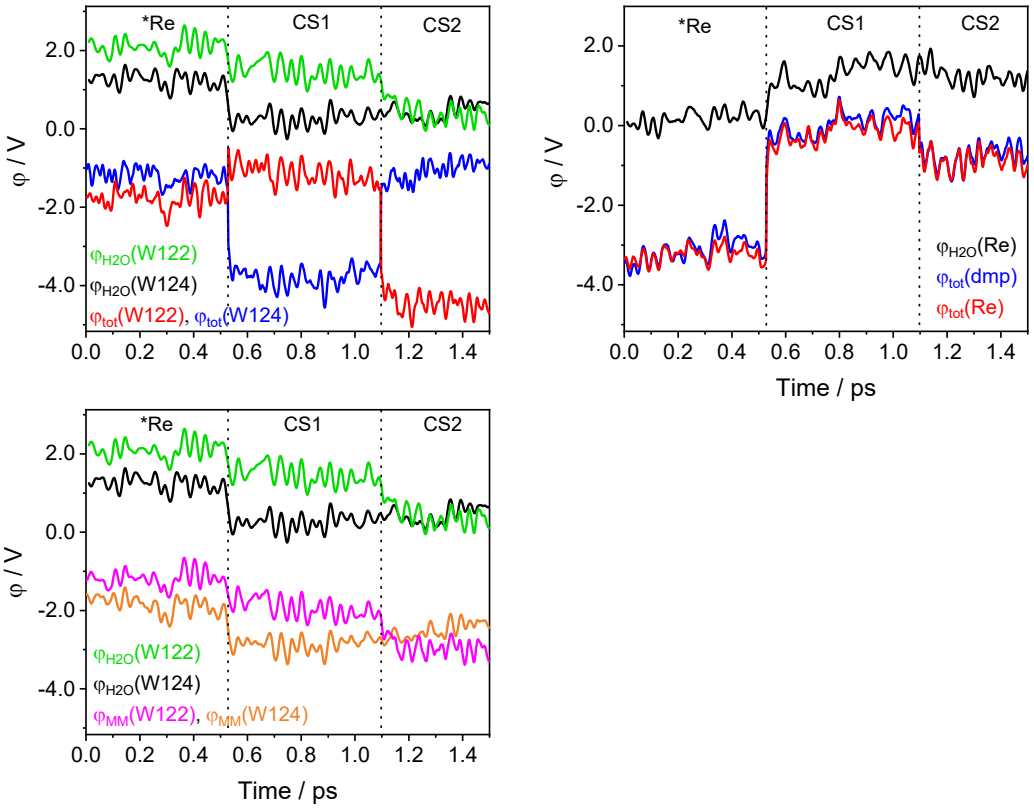

Fig. S31. Electrostatic potential along the B-3 trajectory. Top-left: φ_{H2O} and φ_{tot} at W124 and W122 indoles; Bottom-left: φ_{H2O} and φ_{MM} at W124 and W122 indoles; Top-right: φ_{H2O} and φ_{tot} at the Re complex and φ_{tot} at the dmp ligand. Vertical lines at 528 and 1097 fs mark *Re/CS1 and CS1/CS2 crossings, respectively.

As for other trajectories (Figs. 6, S24), φ_{tot}(W124) drops instantaneously upon *Re←W124 ET (*Re/CS1 boundary) due to a short-range coulombic interaction with $Re^{I}(dmp^{\bullet-})$ and, to a lesser extent, enhanced solvation. φ_{tot}(W122) slightly increases because of the proximity of the positive charge at $W124^{\bullet+}$. φ_{H2O}(W122) slowly decreases in the CS1 state, probably owing to an increasing number and reorientation of water molecules in the W124–W122 region (compare Fig. S29). The second hop, $W124^{\bullet+}$←W122 (CS1/CS2), is accompanied by "instantaneous" switching of φ_{tot} values between W124 and W122. φ_{tot}(W124) returns to its level in *Re before any ET, while φ_{tot}(W122) becomes strongly negative. φ_{H2O}(W122) change is smaller (~25% of the total) and slower, taking ~250 fs to complete. Since the sharp φ(W122) drop occurs only for the total potential, it has to originate from within the QM part of the system, namely from the loss of the positive charge at W124 and from the electrostatic field of $Re^{I}(dmp^{\bullet-})$. φ_{tot}(Re) drops at the CS1/CS2 boundary (right panel) as the positive charge moves farther away from W124 to W122 but is remains higher than in *Re. φ_{H2O}(Re) does not respond to the second hop (right panel). φ_{MM} and φ_{H2O} trajectories at both indoles (bottom-left) and at Re are essentially parallel along the whole B-3 trajectory, ruling out any major contribution from protein motions on this timescale. As in other cases, variations of φ(W) mostly copy φ(NH) for both W122 and W124.

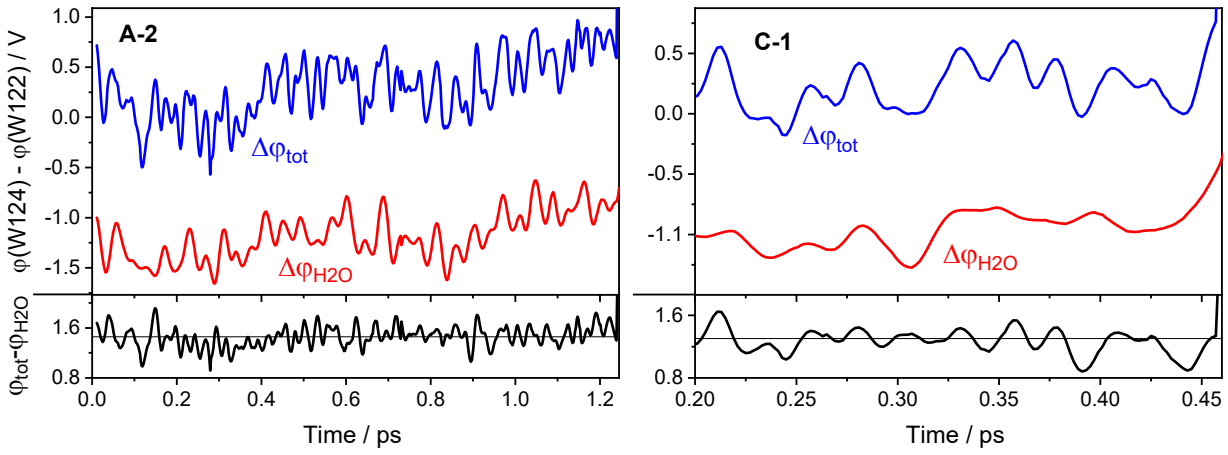

Fig. S32. Difference of electrostatic potentials φ at W124 and W122 indoles, Δφ(W) = φ(W124) – φ(W122), shown along A-2 and C-1 trajectories up to the *Re/CS2 crossing at 1240 (A-2) and 458 fs (C-1). Blue: φ_{tot} generated by all atoms in the system; red: φ_{H2O} generated by water molecules. The two curves increase almost parallel before the *Re/CS2 crossing. Bottom panels (black): Differences between the blue and red curves, $\Delta\varphi_{tot} - \Delta\varphi_{H2O}$, oscillate along their average values, not exhibiting any systematic trend. This observation supports the notion that the $\Delta\varphi_{tot}$ time dependence follows that of $\Delta\varphi_{H2O}$ and that the decisive stabilization of CS2 relative to CS1 is due to solvation by water. The same conclusion holds for $\Delta\varphi_{MM}$. (Note that both φ_{H2O} and φ_{MM} at W122 are larger than at W124 while φ_{tot}(W122) is lower than φ_{tot}(W124). This observation points to the importance of electrostatic interactions within the QM part of the system. In some orientations, coulombic interactions between W124 and the positively charged excited Re complex increase φ_{tot}(W124) well above that at W122.)

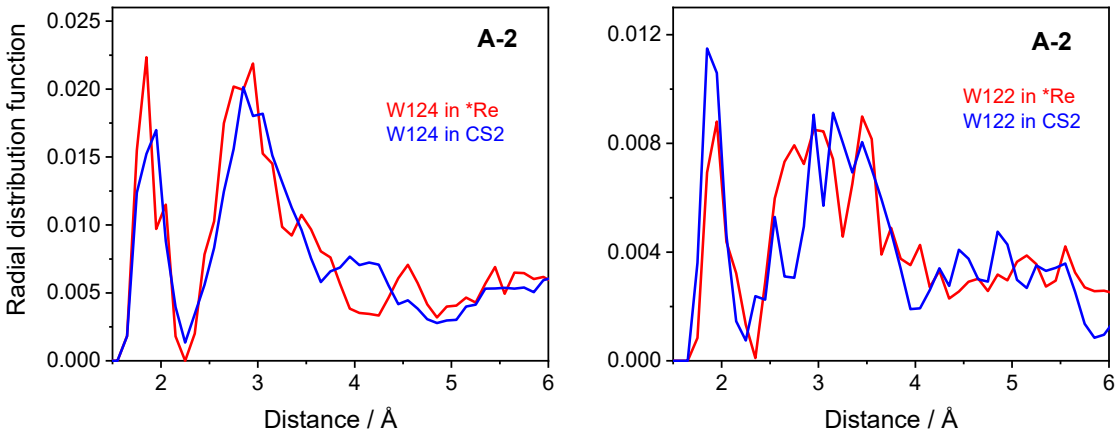

Fig. S33. Water proximal radial distribution function g(*r*) around W124 (left) and W122 (right) indoles in **Re126WW** before (red) and after (blue) the *Re/CS2 crossing calculated along the A-2 trajectory. Conversion to CS2 appears to shift the W124 solvent shell toward $W122^{\bullet+}$, enhancing solvation. (g(*r*) decreases at W124 and increases/shifts closer at W122.)

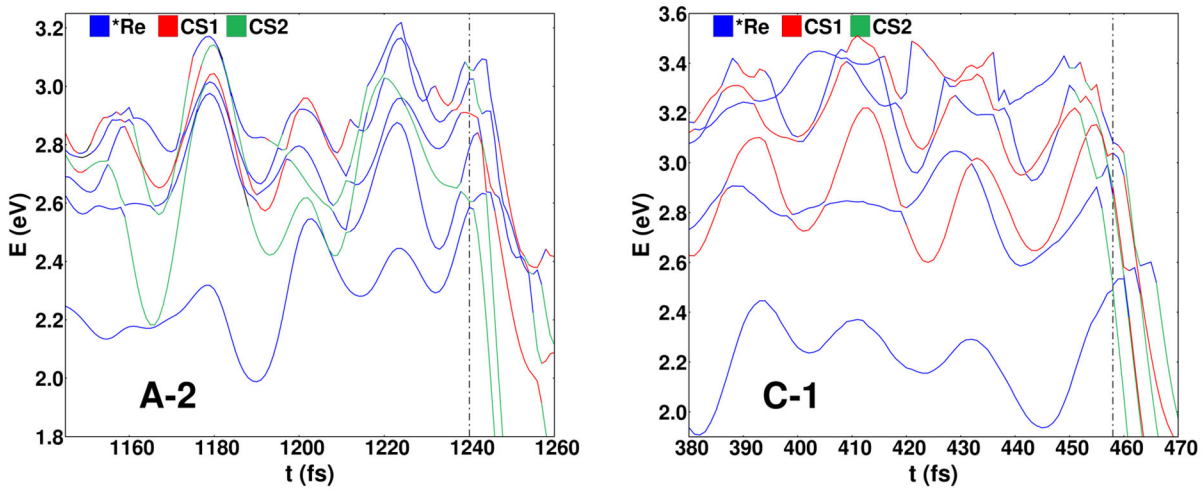

Fig. S34. Energy evolution of six lowest triplet states leading to *Re/CS2 crossing (*Re←W122 ET) in ***Re126WW*** calculated along trajectories A-2 (left) and C-1 (right) shortly before the *Re/CS2 crossing (marked by dash-dot vertical lines). On A-2, note that CS2 approaches *Re several times without crossing. On C-1, the CS2 state originally lies at high energies, out of the set of the six investigated lowest triplet states. Its energy drops sharply during the last 10 fs before crossing, through avoided crossings with CS1 and, finally, with *Re. Neither case shows signs of a temporary *Re – CS1 – CS2 energy alignment needed for flickering resonance (8). (Energies are plotted relative to the singlet **Re126WW** ground state.)

S12. Fourier transform of ΔE(*Re, CS1) reaction coordinate

ΔE trajectories are equivalent to W→*Re reaction coordinates (9) and their Fourier transforms reveal vibrational modes that contribute to the reorganization energy (10). Averaging twelve sufficiently long TDDFT **Re124W** and **Re126WW** trajectories yielded vibrational frequencies 2180±40, 1630±50, 1220±100, and 700±180 cm^{-1}. Multiplication by a scaling factor (11) of 0.9512 (correction for PBE0 functional, 6-31G(d) basis set) produces values 2070, 1550, 1160, 670 cm^{-1} that are attributable to the totally symmetrical in-phase CO stretching (expt. value for *Re: ~2042 cm^{-1}), aromatic (dmp or indole) C-C/N stretching (1550 cm^{-1}) and deformation modes (1160, 670 cm^{-1}) (1, 12-15) The short time-span until the *Re/CS1 crossing does not allow detection of low-frequency protein and collective modes.

S13. Computational procedures

S13.1. System definition

Re124W and **Re126WW** systems were divided into QM (quantum) and MM (classical) parts shown in Fig. 1. The QM regions were defined as $Re(CO)_3$(dmp)(H124)G123W122 and $Re(CO)_3$(dmp)(H126)L125W124G123W122, respectively. They were terminated by linking-H-atoms that were attached to corresponding Cα atoms of the protein backbone. The rest of the system formed the MM region. The protein constructs were solvated with 3342 SPC/E (16, 17) water molecules, resulting in a minimum 6 Å water shell. Two Na^+ cations (18) were added to compensate the charge of the protein chain. Initial structures were based on PDBs 2I7O (**Re124W**) and 6MJS (**Re126WW**).

S13.2. MD simulations

S13.2.1. General procedure

MD simulations started with ground- and excited-state MM/MD, followed by six UKS QM/MM/MD runs that started with geometries and velocities taken from six different snapshots of the excited-state MM/MD trajectories for each (**Re124W, Re126WW)** protein. Finally, we calculated 2 (**Re126W**) or 3 (**Re126WW**) TDDFT QM/MM/MD trajectories using initial structures and velocities taken from 2 or 3 UKS QM/MM/MD snapshots.

S13.2.2. Classical MM/MD simulations

In order to generate uncorrelated configurations of protein sidechains in the vicinity of the QM-region, we first performed classical MM/MD simulations using AMBER 14 software and parameters (19) for the MM part of the system. In order to properly parametrize the QM-region, we developed unique sets of parameters for the Re(im)$(CO)_3$$(dmp)^+$ complex in its ground and lowest-triplet electronic states. The parameter-fitting procedure is described together with the summary of resulting parameters used in MM/MD in section S13.6. DFT (ground-state) or UKS (*Re state) CM5 charges (20) were used for all atoms of the QM region. For the rest of the protein, the ff14SB modifications of parm10 parameters (21, 22) were

employed. The vicinity of the Cu^{I} atom was not investigated in this work. To keep a realistic geometry, we restrained the Cu-ligand distances using data from Table 1 of ref. (23). The SPC/E model was used for explicit water surroundings. Since the Terachem-Amber QM/MM does not support periodic boundary conditions (PBC), we employed harmonic potential on all water molecules to keep them in the spherical water "cap" around the protein, and the whole solvated system was simulated as a large cluster in a gas phase. Electrostatics was accounted for by a very large Coulomb cut-off. MM/MD simulations of the ~60 ns length were performed in an NpT ensemble at an ambient temperature and pressure (300 K, 1 bar) controlled by a Berendsen thermostat and barostat, employing periodic boundary conditions and a 1 fs time-step (24). Relevant MM/MD trajectories are exhibited in Fig. S1 (ground state) and Fig. 2 – top and S3 (*Re excited state).

S13.2.3. QM/MM MD simulations

Molecular dynamics (MD) simulations of lowest triplet states of **Re124W** and **Re126WW** were performed at the QM/MM level in Terachem 1.9 (16, 25) – Amber 14 (19) framework. Description of the MM part remained unchanged and QM-part calculations utilized LANL2DZ quasi-relativistic effective core pseudopotentials and the corresponding optimized set of basis functions for Re (26) and 6-31g(d) polarized double - ζ basis sets for remaining atoms (27). DFT calculations employed the hybrid functional PBE0 (28, 29) together with an empirical dispersion correction (D3) (30). Individual triplet states (*Re, in some test cases also CS1 and CS2) were calculated by the unrestricted KS procedure (UKS). Simultaneous calculations of sets of low-lying triplet states utilized TDDFT with a closed shell reference state (i.e., the system ground state calculated at each time step). Several testing calculations were performed with the long-range-corrected functional CAM-B3LYP (31), see section S6.

Excited-state MD simulations were performed with a 1 fs time step using the SHAKE algorithm (32). Production runs were performed at 300 K employing the Berendsen thermostat (24). The CM-motion was removed every 1 ps. The total simulation times were up to 10 ps for UKS and 1-4 ps for much more computationally demanding TDDFT runs. In order to optimize the use of computational resources, TDDFT calculations were performed on the lowest triplet

excited state. When a state crossing was indicated, MD calculations were rerun with at least 6 roots, starting from geometries and velocities 500-100 fs before the crossing (depending on the trajectory). This procedure was tested on the A-1 trajectory, for which we did not find significant changes upon increasing the number of roots. The multiscale MM/MD→UKS/MM/MD→TDDFT/MM/MD procedure changed stepwise the system configuration in the direction of the transition state, i.e. above the *Re energy minimum. This is documented by g(*r*) around the W124 indole in **Re126WW** shifting at each computational step closer to W124, following the same trend as g(*r*) temporal evolution along *Re sections of TDDFT/MM/MD trajectories (Figs. 5 and S20).

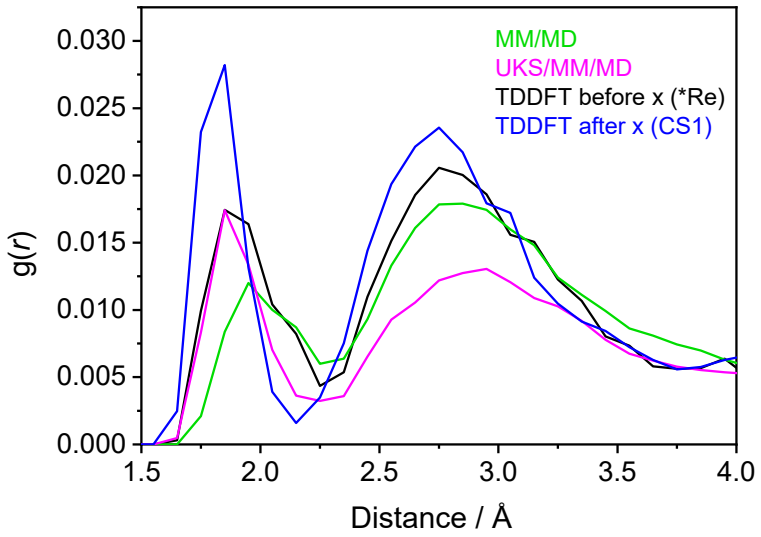

Fig. S35. Water distribution around W124 indole in **Re126WW** at individual computational steps.
Green: g(*r*) averaged over the MM/MD trajectory of the *Re state. Magenta: g(*r*) averaged over all UKS/MD trajectories of the *Re state. Black: g(*r*) averaged over the *Re sections of all TDDFT/MM/MD trajectories showing *Re/CS1. Calculated from the start to the crossing time. Blue: g(*r*) averaged over the CS1 sections of all TDDFT/MM/MD trajectories showing *Re/CS1 crossing. Calculated from the crossing time until the trajectory end.

13.3. Electronic couplings

Calculations of electronic couplings H_{ab} were carried out in the Q-Chem 5.2 program (33) using the fragment charge differences method (FCD) (6) for structures selected from TDDFT

QM/MM/MD trajectories. FCD is similar to the generalized Mulliken-Hush method (GMH) (4, 5) but instead of a dipole moment matrix μ, the donor-acceptor charge-difference matrix Δq was used for diabatization of electronic states:

$$H_{ab} = \frac{(E_2 - E_1)\overline{\Delta q_{12}}}{\sqrt{(\Delta q_{11} - \Delta q_{22})^2 + 4\overline{\Delta q_{12}}^2}} \qquad \text{(S1)},$$

where E_1 and E_2 represent energies of adiabatic states. In this study, the adiabatic states were determined within the corresponding QM parts of **Re124W** and **Re126WW** using TDDFT calculations at the PBE0/6-31G(d) level with LANL2DZ basis set for the Re atom. Six lowest triplet states were considered and the surroundings were included by adding electrostatic interactions with point charges from the MM part into the QM Hamiltonian. In the case of the *Re/CS1 crossing, the acceptor was identified with the Re(im)$(CO)_3$(dmp)$^+$ moiety and the donor with the W122/W124 indole (for **Re124W**/**Re126WW**). For the crossing with the CS2 state in **Re126WW**, the W122 indole represents the donor and either Re(im)$(CO)_3$(dmp)$^+$ (*Re/CS2 crossing) or W124$^{\bullet+}$ (CS1/CS2 crossing) was selected as the acceptor. Characters of TDDFT-calculated electronic states were estimated from the charge localization obtained by the FCD method and only electronic couplings between the ET-relevant states (*Re, CS1, CS2) were taken into account. We also verified that both FCD and GMH methods provide comparable H_{ab} values within the level of theory we employed.

To examine the sensitivity of $|H_{ab}|$ values to the DFT functional, we have compared the PBE0 values (used throughout this work) with those calculated using long-range corrected functionals CAM-B3LYP, ωB97X-D3, and ωB97X-V that also differ in the amount of the HF exchange in the short-range region. Test calculations were performed at the crossing times on **Re124W** trajectories M-2 and L-1, which were chosen because of different electronic structures of the lowest triplet state (*Re): ^{3}IL and ^{3}CT/^{3}IL, respectively. Data in Tab. S3 show that long-range corrected functionals and decreasing HF exchange push the CS1 state up in energy and increase charge delocalization between the excited Re complex and the W122 indole in the CS1 target state. These effects are more prominent on the L-1 trajectory owing to large ^{3}CT participation in the lowest triplet state *Re, resulting in larger $|H_{ab}|$ variations. Importantly, $|H_{ab}|$

values calculated with long-range corrected functionals are comparable to or larger than the PBE0 ones, supporting the adiabaticity conclusion discussed in the main text.

Tab. S3. Electronic coupling between the lowest triplet state T1 (*Re) and low-lying CS1-type states (Target state) in **Re124W** calculated with different DFT functionals. (Q(*Re) and Q(W122) are charges at the *Re(im)$(CO)_3$(dmp)$^+$ complex and the W122 indole, respectively.)

Trajectory M-2 at 157 fs						
Functional	**HF (%)**	**Target state**	**Q(*Re)**	**Q(W122)**	**Principal excitation (%)**	**$\|H_{ab}\|$ (meV)**
PBE0	25	T2 (CS1)	0.866	0.160	75 (HOMO→LUMO)	92.2
CAM-B3LYP	20	T5 (CS1)	0.938	0.095	82 (HOMO→LUMO)	122.7
ωB97X-D3	19.57	T7 (CS1)	0.692	0.338	58 (HOMO→LUMO)	127.7
Trajectory L-1 at 784 fs						
Functional	**HF (%)**	**Target state**	**Q(*Re)**	**Q(W122)**	**Principal excitation (%)**	**$\|H_{ab}\|$ (meV)**
PBE0	25	T2 (CS1)	0.950	0.084	87 (HOMO→LUMO)	54.7
CAM-B3LYP	20	T5 (mixed)	0.577	0.465	51 (HOMO→LUMO)	100.5
		T23 (CS1)	0.854	0.202	51 (HOMO-2→LUMO+1)	39.7
ωB97X-D3	19.57	T18 (CS1)	0.878	0.165	54 (HOMO-2→LUMO)	147.1
		T36 (CS1-type)	0.756	0.294	45 (HOMO-2→LUMO+1)	50.9
ωB97X-V	16.7	T19 (mixed)	0.691	0.342	40 (HOMO-2→LUMO)	103.0
		T39 (CS1)	0.960	0.071	54 (HOMO-2→LUMO+1)	20.4

S13.4. Electrostatic potentials

Electrostatic potentials φ generated by surrounding atoms were evaluated on surfaces surrounding the ET cofactors: Re(im)$(CO)_3$(dmp)$^{+/0}$ and indole (W122/W124) (cf. Fig. S23). The electrostatic potential φ was calculated as the sum of contributions from atoms i with partial charges q_i. (The same procedure was used for QM and MM atoms):

$$\varphi(\vec{r}) = \sum_i \frac{q_i}{|\vec{r_i} - \vec{r}|} \qquad \text{(S2)}.$$

Atomic charges from the Amber force field and Mulliken atomic charges were employed for atoms in the MM and QM parts, respectively. The surfaces were created as envelopes of spheres of scaled van der Waals radii centered at cofactor atoms. The scaling factor of 0.5 was used. In order to calculate the average potential over the envelope, the surface of each sphere

was equidistantly covered by 500 points using a Fibonacci lattice. For this set of points, Delaunay triangulation was performed. In the middle of each triangle belonging to the envelope, the electrostatic potential φ was calculated and eventually averaged over the whole surface, weighted by triangles areas. In addition to whole cofactors, we also examined their smaller moieties (dmp, $(CO)_3$, NH of indole). In this case, the averaging only went over the part of the whole envelope that belonged to spheres centered on atoms of considered groups.

In this way, we evaluated electrostatic potentials originating from all surrounding atoms including atoms from the QM part (φ_{tot}), from all atoms in the MM part (φ_{MM}, protein+water), and from water molecules only (φ_{H2O}). Their differences provided further information on electrostatic interactions within the QM part and on the influence of the rest of the protein and/or the solvent, since the electrostatic potential is additive.

Correlations between the time evolution of the electrostatic potential and the energy difference ΔE between CS1 and *Re states were assessed using Pearson's correlation coefficients:

$$r = \frac{\sum_{i=1}^{n}(\varphi_i - \overline{\varphi})(\Delta E_i - \overline{\Delta E})}{\sqrt{\sum_{i=1}^{n}(\varphi_i - \overline{\varphi})^2}\sqrt{\sum_{i=1}^{n}(\Delta E_i - \overline{\Delta E})^2}} \qquad \text{(S3)}$$

We have examined correlations between ΔE and φ calculated at the same instant of the time evolution and also mutually shifted within the ±20 fs range, attempting to get some idea about causality.

S13.5. Proximal radial distribution functions g(*r*)

The proximal distribution function g(*r*) is a simple-to-implement variation of the radial distribution function (34). The use of proximal distribution functions is beneficial when describing a solution structure (e.g. hydration) near non-spherical molecules where a conventional radial distribution function may lead to significant distortions due to dominant contribution of the large bulk-volume region (7).

Since we were interested in the time evolution of hydration of the QM-domain, we have defined the proximal regions around its ET-relevant groups, namely dmp, the three CO ligands, and the two indoles (W122, W124). We have measured the closest distance between water oxygen atoms and atoms of the selected group. Each water molecule was accounted solely to its closest residue *i*, and the $g_i(r)$ was determined as an ensemble average over the trajectory (set of configurations) of interest. This "exclusive" approach was further time-resolved, so that the time-evolution of the hydration was investigated. Our main focus was on the vicinity of the electronic-state crossing. Here, the temporary $g_i(r, t_{min} < t < t_{min}+dt)$ was obtained by averaging only over a certain time-window (100 or 20 fs) of the trajectory. System configurations were saved every 1 fs, which yielded approximately 3000 samples for analysis over a 3 ps simulation. Analyses were performed using our in-house Python implementation.

S13.6. MM parametrization of ground- and excited-state $[Re(im)(CO)_3(dmp)]^+$

In the first instance, solution structures of ground and *Re excited-state **Re124W** and **Re126WW** were obtained by classical MM/MD simulations that required developing new sets of bonding and nonbonding parameters for $Re(im)(CO)_3(dmp)^+$ in the ground- and lowest triplet states (im = imidazole, a part of H124 or H126). (Using standard GAFF (General Amber Force Field) parameters was not sufficient because coordination to the Re atom strongly affects charge distribution and bonding in the dmp and im ligands and more than one type of aromatic carbon atom had to be used. Moreover, GAFF parameters for the Re atoms and inorganic carbonyls are not available.)

The labeling of different types of atoms within dmp and im ligands is depicted in Fig. S36 and their positions are listed in Tab. S4. For this set of 22 atom types, we have determined the atomic charges as well as all force constants, equilibrium values of bonding terms, and parameters of Lennard-Jones (LJ) potentials associated with the Re complex.

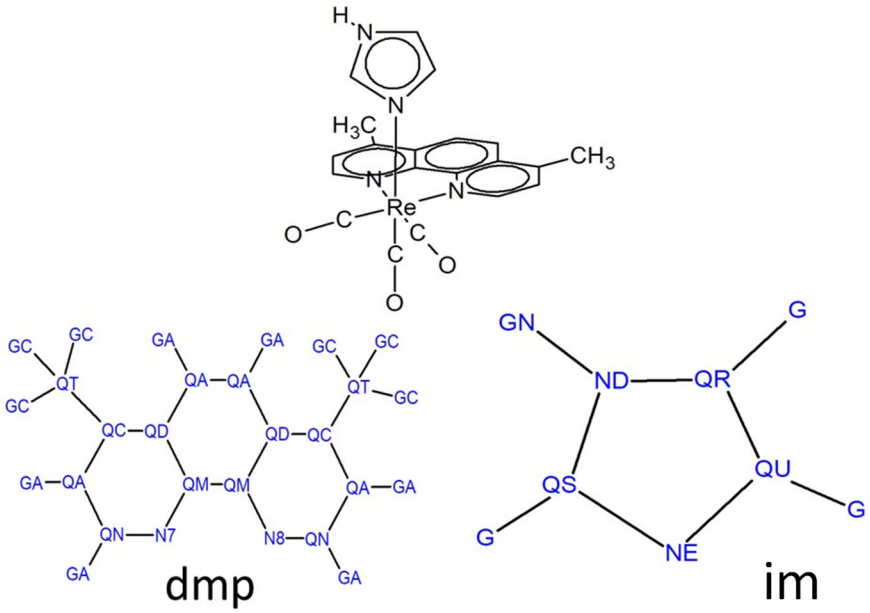

Fig. S36. Structure of the $[Re(im)(CO)_3(dmp)]^+$ complex and labeling of atom types within dmp and im ligands. C-carbonyl atoms in the equatorial position are labeled Q7 and Q8, the axial one Q9. Oxygen atoms of the carbonyls are described by one type OQ.

Tab. S4. Atomic Cartesian coordinates of the $[Re^{I}(im)(CO)_3(dmp)]^+$ structure optimized at the PBE0/6-311+G(d)/PCM-H_2O level. Atom types assigned according to Fig. S36.

	Fragment	Atom type	Element	xyz		
1	His	QR	C	-0.922699	-0.000472	3.874928
2	His	ND	N	-2.280557	-0.000436	3.696782
3	His	GN	H	-2.978015	-0.000509	4.428168
4	His	QS	C	-2.539975	-0.000292	2.381949
5	His	G	H	-3.535265	-0.000237	1.964826
6	His	NE	N	-1.406139	-0.000214	1.691551
7	His	QU	C	-0.386876	-0.000335	2.619891
8	His	G	H	0.653147	-0.000311	2.334377
9	Re	Re	Re	-1.277489	0.000060	-0.494741
10	dmp	N8	N	0.423267	-1.326407	-0.239821
11	dmp	QN	C	0.392958	-2.655361	-0.219845
12	dmp	GA	H	-0.581864	-3.121397	-0.307275
13	dmp	QA	C	1.545785	-3.435973	-0.098889
14	dmp	GA	H	1.442469	-4.515917	-0.090076
15	dmp	QC	C	2.793651	-2.847992	0.005106
16	dmp	QT	C	4.033925	-3.673951	0.130818
17	dmp	GC	H	4.562766	-3.449125	1.064193
18	dmp	GC	H	4.727430	-3.470369	-0.693084

19	dmp	GC	H	3.794913	-4.739410	0.121265
20	dmp	QD	C	2.845428	-1.426330	-0.009067
21	dmp	QA	C	4.060613	-0.681187	0.100099
22	dmp	GA	H	4.999736	-1.216328	0.188226
23	dmp	QA	C	4.060626	0.681115	0.100213
24	dmp	GA	H	4.999757	1.216225	0.188430
25	dmp	QD	C	2.845452	1.426297	-0.008827
26	dmp	QC	C	2.793701	2.847959	0.005585
27	dmp	QT	C	4.033990	3.673874	0.131429
28	dmp	GC	H	3.794987	4.739338	0.122172
29	dmp	GC	H	4.562904	3.448797	1.064702
30	dmp	GC	H	4.727429	3.470503	-0.692583
31	dmp	QA	C	1.545845	3.435979	-0.098317
32	dmp	GA	H	1.442549	4.515923	-0.089322
33	dmp	QN	C	0.393005	2.655407	-0.219401
34	dmp	GA	H	-0.581809	3.121474	-0.306754
35	dmp	N7	N	0.423292	1.326456	-0.239598
36	dmp	QM	C	1.635915	0.715101	-0.131748
37	dmp	QM	C	1.635901	-0.715091	-0.131867
38	CO(eq)	Q7	C	-2.623315	-1.349694	-0.637772
39	CO(eq)	O	O	-3.421601	-2.187744	-0.721469
40	CO(eq)	Q8	C	-2.623300	1.349860	-0.637531
41	CO(eq)	O	O	-3.421639	2.187884	-0.720983
42	CO(ax)	Q9	C	-1.082735	0.000113	-2.398290
43	CO(ax)	O	O	-0.969076	0.000795	-3.552219

In order to obtain the best set of parameters for the $[Re(im)(CO)_3(dmp)]^+$ complex and its composing atoms, we generated a set of different geometries produced from the DFT-optimized $[Re(im)(CO)_3(dmp)]^+$ structure (to fit intramolecular parameters) and systems containing the complex and a small "test" molecule (to fit atomic charges and LJ parameters describing intermolecular interactions and interactions between not-directly bonded atoms of the complex). 20 dipeptides consisting of a glycine and one of the 20 amino acids or a water molecule were chosen as test molecules for the sake of modeling relevant surroundings of the Re complex. Rigid test molecules were then moved relative to the rigid optimized complex in randomly selected directions and orientations. The exact point to which they were pulled was chosen randomly within a sphere of a 2 Å radius centered at an atom of the complex – either the axial-carbonyl oxygen, imidazole Nδ, a dmp aromatic carbon atom, or (in one quarter of

scans) a randomly selected atom. In this way, 9559 systems were prepared. Interaction energies between the complex and test molecules were then calculated by DFT and subsequently used for fitting of non-bonding parameters in the MM energy expression (eq. S4).

Structures of the Re complex for fitting bonding parameters (force constants, equilibrium bond distances, angles, and dihedral angles) were prepared in four different ways: a) scanning potential energy surfaces (PES) along normal vibrational modes; b) from PES for stretching Re-ligand bonds or imidazole rotation relative to the rest of the complex; c) geometries from DFT QM/MM/MD dynamics of the Re complex solvated with explicit (MM) water; and d) structures generated from MM/MD iteratively using parameters fitted in the previous step. Including the latter structures helped us minimizing weak sites of previous parameter sets in two iterative steps. Energies of all these structures were then calculated by DFT and used in parameter fitting.

All DFT calculations of $[Re(im)(CO)_3(dmp)]^+$ structures and energies used in the parameter-fitting procedure were carried out with G16 (35) at the B3LYP-GD3BJ/6-31++G(d,p)/SDD level and using the Stuttgart-Dresden averaged relativistic pseudopotential for the Re atom. Structures for PES scans along the vibrational normal modes (of the found minimum) were based on frequency analysis for the lowest-energy geometry of the Re complex. "Non-bonding" rigid PES of systems consisting of dipeptides or a water molecule and the Re complex were calculated using a smaller 6-31+G(d)/SDD basis. Structures of the complex and "test" molecules stayed rigid in their respective optimal geometries over the whole scans. Configurations with too close contacts, i.e., where atoms were closer than the sum of their covalent radii, were excluded. All these calculations were performed for systems in the gas phase. Classical MM/MD (c), and also QM/MM/MD (d) simulations of the Re complex in an explicit water solution served for verification of the newly generated parameters (calculation of radial distribution functions (RDFs) and velocity power spectra) as well as a source of geometries subsequently used in the fit. They were carried out in the Amber 14 (19), where G16 (35) was called as the external program for DFT calculations of energies and forces. The QM part contained only the Re complex while the solvent was described at an MM level using the TIP3P water model. Energies and forces in the QM part were calculated at the

B97D/LANL2DZ level using density fitting and the electrostatic interaction between QM and MM part was included by employing electronic embedding.

Fitting procedure was performed using home-developed software. In order to find the best set of parameters, the Levenberg-Marquardt algorithm (36, 37) was employed to minimize the sum of squared deviations between MM and QM energy differences for the structures generated as described above. As we tried to find parameters consistent with Amber force fields, the MM energy expression was considered in the form:

$$E_{MM} = \sum_{i}^{bonds} \frac{k_i^B}{2}(r_i - r_i^0)^2 + \sum_{i}^{angles} \frac{k_i^A}{2}(\phi_i - \phi_i^0)^2 + \sum_{i}^{dihedrals} \frac{k_i^D}{2}(1 + cos(n_i\theta_i - \theta_i^0)) + \frac{1}{2}\sum_{i}^{atoms}\sum_{j\neq i}^{atoms}\left(\frac{q_i q_j}{r_{ij}} + \epsilon_{ij}\left(\left(\frac{r_{ij}^0}{r_{ij}}\right)^{12} - 2\left(\frac{r_{ij}^0}{r_{ij}}\right)^{6}\right)\right) \quad \text{(S4)}$$

The first three terms represent bonding interactions - the first sum describes bond stretching, the second one bending of bonding angles, and the following one is associated with dihedral angles. The last term includes electrostatic interactions and LJ potentials describing non-bonding interactions where the 1-4 terms are scaled in accord with the Amber program (i.e., the electrostatic term is divided by the factor of 1.20 and the LJ potential by 2.00). $r_i^0, \phi_i^0, \theta_i^0$ represent equilibrium bond lengths, angles, and dihedral angles, respectively. k_i^B, k_i^A, k_i^D are corresponding force constants. q stands for atomic charges, r_{ij} interatomic distances, ϵ_{ij} stands for the depth of the LJ potential and r_{ij} is the position of its minimum.

The requirement to minimize the sum of the deviations for considered geometries $\mathbf{x_i}$

$$S(\boldsymbol{\alpha}) = \sum_{i}^{geometries} w_i \left(\Delta E_{QM}(\mathbf{x}_i) - E_{MM}(\mathbf{x}_i, \boldsymbol{\alpha})\right)^2 \quad \text{(S5)}$$

using expansion of the expression for the MM energy around an initial set of the parameters $\boldsymbol{\alpha}$ to the first order:

$$E_{MM}(\mathbf{x}_i, \boldsymbol{\alpha} + \boldsymbol{\delta}) \approx E_{MM}(\mathbf{x}_i, \boldsymbol{\alpha}) + \mathbf{J}(\mathbf{x}_i, \boldsymbol{\alpha})\boldsymbol{\delta} \quad ; \qquad \mathbf{J}(\mathbf{x}_i, \boldsymbol{\alpha}) = \frac{\partial E_{MM}(\mathbf{x}_i, \boldsymbol{\alpha})}{\partial \boldsymbol{\alpha}} \qquad \text{(S6)}$$

leads to the final equation for the shifts $\boldsymbol{\delta}$ of the parameters:

$$[\mathbf{J}^T\mathbf{W}\mathbf{J} + \lambda diag(\mathbf{J}^T\mathbf{W}\mathbf{J})]\boldsymbol{\delta} = \mathbf{J}^T\mathbf{W}[\boldsymbol{\Delta}\mathbf{E}_{QM} - \mathbf{E}_{MM}]. \qquad \text{(S7)}$$

Seeking the best set of the parameters $\boldsymbol{\alpha}$ proceeded in an iterative way and the LAPACK libraries were used for solving equation S7. Individual deviations between QM and MM energies in the sum in equation S5 can be scaled by weights w_i in order to emphasize the importance of some structures. In equation S7, the weights w_i are included in the matrix $\mathbf{W}$. The second term on the left side of equation S7 serves to influence the speed of convergence via the damping parameter λ.

Fitted values of force constants and equilibrium bonding parameters are listed in Tab. S5; fitted LJ parameters are summarized in Tab. S6. Test MM/MD calculations showed unrealistically large deviations of Re-N and Re-C bond lengths from their equilibrium values. Therefore, force constants of Re-ligand bonds were fixed at the value of 600 kcal·mol^{-1}·Å^{-2}, remaining force constants values were used as stated in Tab. S5.

Tab. S5. Equilibrium bond parameters and fitted force constants
a. Equilibrium bond lengths (in Å) and force constants (in kcal·mol^{-1}·Å^{-2})

Bond type	Force const.	Bond length	Bond type	Force const.	Bond length
Re-NE	126.52	2.190	Q8-OQ	936.07	1.161
Re-N8	66.02	2.172	Q7-OQ	936.07	1.161
Re-N7	66.02	2.172	QN-QA	460.01	1.401
Re-Q9	368.42	1.913	QN-GA	412.16	1.084
Re-Q8	318.99	1.911	QA-QC	490.87	1.388
Re-Q7	318.99	1.911	QA-GA	411.90	1.085
NE-QS	329.11	1.330	QC-QD	349.33	1.427
NE-QU	283.68	1.386	QC-QT	277.17	1.502
N8-QN	447.86	1.335	QD-QM	605.74	1.414
N8-QM	397.32	1.369	QD-QA	230.34	1.434
N7-QM	499.59	1.369	QM-QM	545.21	1.436
N7-QN	495.94	1.335	QA-QA	154.70	1.366
ND-QS	578.11	1.353	QR-QU	540.92	1.369
ND-QR	529.91	1.380	QR-G	346.62	1.078
ND-GN	587.17	1.011	QU-G	519.97	1.077
QS-G	435.10	1.079	QT-GC	377.01	1.091
Q9-OQ	879.51	1.157	CT-QR	317.00	1.504

Tab. S5 cont'd.

b. Equilibrium angles (in deg) and force constants (in kcal·mol^{-1}·rad^{-2})

Angle type	Force const.	Equil. angle	Angle type	Force const.	Equil. angle
NE-Re-N8	81.45	87.597	N8-QN-GA	44.63	115.208
NE-Re-N7	81.45	87.597	QA-QN-GA	23.57	123.317
NE-Re-Q9	25.18	177.413	QN-QA-QC	66.45	120.123
NE-Re-Q8	14.10	90.579	QN-QA-GA	70.48	120.117
NE-Re-Q7	14.10	90.579	QC-QA-GA	22.46	122.143
N8-Re-N7	128.41	75.102	QA-QC-QD	21.10	117.241
N8-Re-Q9	45.51	92.521	QA-QC-QT	77.56	120.820
N8-Re-Q8	5.00	172.326	QD-QC-QT	33.28	122.907
N8-Re-Q7	16.44	98.119	QC-QD-QM	75.96	117.114
N7-Re-Q9	65.25	87.618	QC-QD-QA	103.52	125.299
N7-Re-Q8	16.44	98.119	QM-QD-QA	74.15	117.697
N7-Re-Q7	64.55	168.092	N8-QM-QD	68.28	122.917
Q9-Re-Q8	63.19	91.234	N8-QM-QM	96.70	117.689
Q9-Re-Q7	63.19	91.234	QD-QM-QM	36.53	120.369
Q8-Re-Q7	27.28	90.722	N7-QM-QM	96.70	117.689
Re-NE-QS	35.22	127.740	N7-QM-QD	68.28	122.917
Re-NE-QU	5.00	126.671	N7-QN-QA	25.79	123.053
QS-NE-QU	158.86	105.815	N7-QN-GA	44.63	115.208
Re-N8-QN	5.66	126.056	QD-QA-QA	78.34	122.093
Re-N8-QM	5.00	114.565	QD-QA-GA	47.63	119.523
QN-N8-QM	64.42	120.645	QA-QA-GA	27.54	118.759
Re-N7-QM	27.37	114.980	ND-QR-QU	81.07	105.710
Re-N7-QN	5.00	125.425	ND-QR-G	68.99	120.621
QM-N7-QN	100.79	118.848	QU-QR-G	5.00	132.593
QS-ND-QR	138.94	108.407	NE-QU-QR	122.73	108.999
QS-ND-GN	28.64	124.388	NE-QU-G	68.26	121.739
QR-ND-GN	28.12	122.782	QR-QU-G	13.45	129.517
NE-QS-ND	57.80	111.258	QC-QT-GC	42.41	110.046
NE-QS-G	5.00	125.981	GC-QT-GC	35.69	108.721
ND-QS-G	53.21	122.749	HC-CT-QR	50.00	109.500
Re-Q9-OQ	31.82	181.187	CT-QR-ND	70.00	120.000

Re-Q8-OQ	64.91	177.229	CT-QR-QU	70.00	120.000
Re-Q7-OQ	59.71	175.045	CX-CT-QR	63.00	113.100
N8-QN-QA	25.79	123.053			

Tab. S5 cont'd.

c. Dihedral parameters: Energy barriers for rotations (kcal·mol^{-1}), equilibrium dihedral angles (deg) and potential periodicity

Dihedral type	Barrier/2	Phase shift	Period.	Dihedral type	Barrier/2	Phase shift	Period.
N8-Re-NE-QS	0.010	322.405	1.00	Re-N7-QM-QD	0.010	180.000	2.00
N8-Re-NE-QU	0.010	142.396	1.00	QN-N7-QM-QM	7.628	180.000	2.00
N7-Re-NE-QS	0.010	37.562	1.00	QN-N7-QM-QD	5.293	180.000	2.00
N7-Re-NE-QU	0.010	217.553	1.00	Re-N7-QN-QA	8.591	180.000	2.00
Q9-Re-NE-QS	0.010	359.976	1.00	Re-N7-QN-GA	1.775	180.000	2.00
Q9-Re-NE-QU	0.043	179.966	1.00	QM-N7-QN-QA	5.505	180.000	2.00
Q8-Re-NE-QS	0.126	134.585	1.00	QM-N7-QN-GA	7.842	180.000	2.00
Q8-Re-NE-QU	0.094	314.576	1.00	QR-ND-QS-NE	14.216	180.000	2.00
Q7-Re-NE-QS	0.010	225.382	1.00	QR-ND-QS-G	0.010	180.000	2.00
Q7-Re-NE-QU	0.010	45.373	1.00	GN-ND-QS-NE	2.434	180.000	2.00
NE-Re-N8-QN	0.010	87.485	1.00	GN-ND-QS-G	1.555	180.000	2.00
NE-Re-N8-QM	0.010	269.601	1.00	QS-ND-QR-QU	13.601	180.000	2.00
N7-Re-N8-QN	0.010	0.594	1.00	QS-ND-QR-G	0.010	180.000	2.00
N7-Re-N8-QM	0.010	182.710	1.00	GN-ND-QR-QU	2.660	180.000	2.00
Q9-Re-N8-QN	0.010	269.284	1.00	GN-ND-QR-G	1.723	180.000	2.00
Q9-Re-N8-QM	0.010	91.399	1.00	N8-QN-QA-QC	7.781	180.086	2.00
Q8-Re-N8-QN	0.631	16.352	1.00	N8-QN-QA-GA	4.908	180.000	2.00
Q8-Re-N8-QM	0.550	198.467	1.00	GA-QN-QA-QC	2.596	180.000	2.00
Q7-Re-N8-QN	25.071	178.341	1.00	GA-QN-QA-GA	4.351	180.000	2.00
Q7-Re-N8-QM	25.420	0.457	1.00	QN-QA-QC-QD	3.137	180.000	2.00
NE-Re-N7-QM	0.010	90.402	1.00	QN-QA-QC-QT	4.400	180.000	2.00
NE-Re-N7-QN	0.010	272.516	1.00	GA-QA-QC-QD	5.579	180.000	2.00
N8-Re-N7-QM	0.010	177.291	1.00	GA-QA-QC-QT	5.105	180.000	2.00
N8-Re-N7-QN	0.010	359.405	1.00	QA-QC-QD-QM	8.909	180.000	2.00
Q9-Re-N7-QM	3.731	268.603	1.00	QA-QC-QD-QA	0.639	180.000	2.00
Q9-Re-N7-QN	0.010	90.716	1.00	QT-QC-QD-QM	3.800	180.000	2.00
Q8-Re-N7-QM	0.010	359.546	1.00	QT-QC-QD-QA	3.514	180.000	2.00

Q8-Re-N7-QN	0.010	181.660	1.00	QA-QC-QT-GC	0.010	180.000	3.00
Q7-Re-N7-QM	0.271	161.545	1.00	QD-QC-QT-GC	0.379	0.000	3.00
Q7-Re-N7-QN	0.182	343.658	1.00	QC-QD-QM-N8	4.569	180.000	2.00
NE-Re-Q9-OQ	0.586	180.145	1.00	QC-QD-QM-QM	1.809	180.000	2.00
N8-Re-Q9-OQ	0.010	217.625	1.00	QA-QD-QM-N8	0.010	180.000	2.00
N7-Re-Q9-OQ	0.010	142.649	1.00	QA-QD-QM-QM	4.248	180.000	2.00
Q8-Re-Q9-OQ	0.010	45.524	1.00	QC-QD-QA-QA	0.010	180.000	2.00
Q7-Re-Q9-OQ	0.010	314.750	1.00	QC-QD-QA-GA	1.677	180.000	2.00
NE-Re-Q8-OQ	0.010	123.748	1.00	QM-QD-QA-QA	0.138	180.000	2.00
N8-Re-Q8-OQ	0.010	194.513	1.00	QM-QD-QA-GA	1.751	180.000	2.00
N7-Re-Q8-OQ	0.010	209.836	1.00	N8-QM-QM-N7	14.294	180.000	2.00
Q9-Re-Q8-OQ	0.010	301.649	1.00	N8-QM-QM-QD	0.010	180.000	2.00
Q7-Re-Q8-OQ	0.010	32.383	1.00	QD-QM-QM-N7	10.833	180.000	2.00
NE-Re-Q7-OQ	0.010	236.296	1.00	QD-QM-QM-QD	3.068	180.000	2.00
N8-Re-Q7-OQ	0.010	150.210	1.00	N7-QM-QD-QC	0.924	180.000	2.00
N7-Re-Q7-OQ	0.302	165.522	1.00	N7-QM-QD-QA	0.010	180.000	2.00
Q9-Re-Q7-OQ	0.010	58.396	1.00	QC-QA-QN-N7	6.130	180.000	2.00
Q8-Re-Q7-OQ	0.010	327.662	1.00	GA-QA-QN-N7	0.010	180.000	2.00
Re-NE-QS-ND	31.757	0.003	1.00	QD-QA-QA-QD	9.516	180.000	2.00
Re-NE-QS-G	0.010	180.000	2.00	QD-QA-QA-GA	9.488	180.000	2.00
QU-NE-QS-ND	4.620	180.000	2.00	GA-QA-QA-GA	1.181	180.003	2.00
QU-NE-QS-G	11.835	180.000	2.00	ND-QR-QU-NE	5.924	180.000	2.00
Re-NE-QU-QR	3.566	180.000	2.00	ND-QR-QU-G	0.010	180.000	2.00
Re-NE-QU-G	0.788	180.000	2.00	G -QR-QU-NE	5.972	180.000	2.00
QS-NE-QU-QR	16.218	180.000	2.00	G -QR-QU-G	0.010	180.000	2.00
QS-NE-QU-G	10.210	180.000	2.00	HC-CT-QR-ND	0.000	0.000	2.00
Re-N8-QN-QA	0.010	180.000	2.00	HC-CT-QR-QU	0.000	0.000	2.00
Re-N8-QN-GA	1.058	180.000	2.00	HC-CT-QR-ND	0.000	0.000	2.00
QM-N8-QN-QA	0.010	180.000	2.00	HC-CT-QR-QU	0.000	0.000	2.00
QM-N8-QN-GA	4.155	180.000	2.00	CT-QR-ND-GN	1.400	180.000	2.00
Re-N8-QM-QD	0.010	180.000	2.00	CT-QR-ND-QS	1.400	180.000	2.00
Re-N8-QM-QM	0.977	180.000	2.00	CT-QR-QU-NE	5.150	180.000	2.00
QN-N8-QM-QD	0.010	180.000	2.00	CT-QR-QU-G	5.150	180.000	2.00
QN-N8-QM-QM	0.010	180.000	2.00	CX-CT-QR-ND	0.000	0.000	2.00
Re-N7-QM-QM	2.772	180.000	2.00	CX-CT-QR-QU	0.000	0.000	2.00

Tab. S6. Fitted Lennard-Jones parameters: Equilibrium distances in Å and depth of the minimum in kcal·mol^{-1}.

Atom Type	$r_0/2$	ϵ	Atom Type	$r_0/2$	ϵ
Re	3.934	0.500	QC	1.843	0.419
NE	1.484	0.500	QD	1.568	0.258
N8	1.614	0.500	QM	1.534	0.500
N7	1.614	0.500	QR	1.831	0.098
ND	1.690	0.129	QU	1.628	0.500
QS	1.742	0.227	OQ	1.566	0.049
Q9	1.024	0.500	QT	1.678	0.292
Q8	1.544	0.085	GA	1.071	0.010
Q7	1.544	0.085	GN	0.500	0.216
QN	1.730	0.072	G	1.094	0.010
QA	1.813	0.069	GC	1.097	0.010

Atomic charges. Charges amount to the most important part of the force field with respect to describing intermolecular interactions. The fitting procedure described in the previous section provided a set of "fitted charges" at $[Re^{I}(im)(CO)_3(dmp)]^+$ atoms (Fig. S6) that were compared with atomic charges calculated using several different QM approaches at the optimized geometry: Natural Population Analysis (NPA) (38, 39), Hirshfeld analysis (40), CM5 (20), and RESP (41, 42). Fitting was initially started using in eq. S4 either NPA or RESP sets of charges. The latter was selected as the method to calculate atomic charges recommended in the Amber manual (19). However, we found that RESP strongly over-polarized atomic charges, particularly at the Re atom and CO ligands. Atomic charges producing the smallest deviations in the fitting procedure ("Fitted" in Tab. S7) were therefore obtained starting from the NPA set. CM5 population analysis was the only one that did not produce overpolarized carbonyl groups. Hence, in ground and excited-state MM/MD simulations of whole **Re124W** and **Re126WW** systems (e.g. Fig. 2-top. Figs. S1 and S3), we have used CM5 charges (Tab. S7) instead of the fitted ones. (CM5 charges were used for the whole QM part, not only the Re complex.) All other MM parameters were used as obtained by the fitting procedure described above (eqs. S4-S7,

Tabs. S5-6). This parametrization was validated (for the ground state) by a good match between measured and calculated UV-vis spectra of MM/MD-simulated solution structures of $[Re^{I}(im)(CO)_3(dmp)]^+$, as well as of **Re124W** and **Re126WW** in water (Fig. S2). It should be noted that atomic charges (non-bonding interactions) play a crucial role in determining the absorption spectrum of the Re complex bound to proteins where the dmp ligand interacts with the indole moiety of the adjacent tryptophan residue, especially, when these moieties are stacked such as in **Re124W**.

***Re excited-state parametrization.** For MD/MM simulations of **Re124W** and **Re126WW** in the *Re triplet state, we have adopted force constants for bonding terms along with LJ parameters from the ground state parametrization (to mitigate high demands of excited-state QM calculations). On the other hand, equilibrium lengths and angles of Re-ligand bonds and bonds within dmp were taken from the UKS lowest-triplet structure optimized in the C_s symmetry (Tab. S8). Excited-state CM5 atomic charges were used for the whole QM part of the system, assuming C_s symmetry for Re complex. (Note that UKS-optimized *Re structure showed asymmetric Re-N7 and Re-N8 bond lengths and the im plane oriented approximately parallel with one of the Re-N bonds. In order to avoid the preference of one specific orientation in excited-state MM/MD runs, we have calculated UKS excited-state geometrical parameters and CM5 charges in the C_s symmetry.)

Tab. S7. Atomic charges for $[Re^{I}(im)(CO)_3(dmp)]^+$ used in MM simulations of the ground- and *Re states. They were determined using the CM5 analysis (20) at the UKS PBE0-GD3BJ/6-31+G(d)/PCM-H_2O level of the whole QM parts of **Re124W** and **Re126WW** systems solvated with a water continuum. Atoms are listed in the same order as in Tab. S4. CM5 charges for *Re were obtained by UKS calculation assuming the C_s symmetry of the Re complex. CM5 charges for the rest of the QM parts are available upon request.
"Fitted" charges were obtained by the procedure described by equations S4-S7, using NPA charges as the initial guess. "Fitted" charges are listed only for comparison since they were not used in subsequent MM/MD simulations.

	Atom type	GS (ReW)	GS(ReWW)	*Re(ReW)	*Re(ReWW)	Fitted (GS)
1	QR	0.0914	0.0904	0.1058	0.0950	-0.1069
2	ND	-0.3834	-0.3788	-0.3610	-0.3719	-0.3816

3	GN	0.3714	0.3666	0.3880	0.3688	0.3548
4	QS	0.1696	0.1697	0.1784	0.1802	-0.0070
5	G	0.1635	0.1637	0.1598	0.1605	0.2449
6	NE	-0.3470	-0.3647	-0.3622	-0.3704	-0.3657
7	QU	0.0049	0.0028	0.0059	0.0080	-0.0362
8	G	0.1347	0.1318	0.1465	0.1340	0.2893
9	Re	0.6318	0.6355	0.7522	0.7541	0.2760
10	N8	-0.3442	-0.3335	-0.3603	-0.3808	-0.5515
11	QN	0.0817	0.0801	0.0696	0.0171	-0.1051
12	GA	0.1467	0.1415	0.1403	0.1176	0.2729
13	QA	-0.0809	-0.0786	-0.1074	-0.0900	0.2258
14	GA	0.1308	0.1170	0.1201	0.1104	0.0738
15	QC	0.0335	0.0365	0.0156	0.0066	-0.2327
16	QT	-0.2152	-0.2194	-0.2211	-0.2295	-0.4416
17	GC	0.1178	0.1103	0.1085	0.0949	0.1786
18	GC	0.1072	0.1075	0.1051	0.0905	0.1786
19	GC	0.1145	0.1033	0.1080	0.0925	0.1786
20	QD	0.0061	0.0073	-0.0066	0.0047	0.2336
21	QA	-0.0682	-0.0751	-0.0805	-0.0744	-0.2698
22	GA	0.1264	0.1266	0.1259	0.1174	0.1770
23	QA	-0.0681	-0.0751	-0.0831	-0.0668	-0.2698
24	GA	0.1249	0.1273	0.1216	0.1199	0.1770
25	QD	0.0091	0.0053	-0.0073	-0.0048	0.2336
26	QC	0.0354	0.0331	0.0016	0.0330	-0.2327
27	QT	-0.2216	-0.2152	-0.2251	-0.2131	-0.4416
28	GC	0.1047	0.1122	0.1001	0.1027	0.1786
29	GC	0.0969	0.1128	0.1036	0.1060	0.1786
30	GC	0.1123	0.1135	0.1038	0.1084	0.1786
31	QA	-0.0769	-0.0747	-0.1090	-0.0927	0.2258
32	GA	0.1341	0.1314	0.1226	0.1213	0.0738
33	QN	0.0746	0.0804	0.0245	0.0778	-0.1051
34	GA	0.1344	0.1401	0.1289	0.1349	0.2729
35	N7	-0.3495	-0.3331	-0.3915	-0.3525	-0.5515
36	QM	0.1300	0.1265	0.0818	0.1087	0.2109
37	QM	0.1147	0.1251	0.0876	0.0985	0.2109
38	Q7	0.0823	0.0653	0.1495	0.0733	0.2286
39	O	-0.1913	-0.1961	-0.1207	-0.1842	-0.1662
40	Q8	0.0513	0.0457	0.1177	0.0829	0.2286
41	O	-0.2060	-0.2075	-0.1385	-0.1659	-0.1662
42	Q9	0.0565	0.0621	0.0784	0.1156	0.2286
43	O	-0.2044	-0.1984	-0.1840	-0.1531	-0.1662

Tab. S8. Selected DFT (PBE0/6-311+G(d)/PCM-H_2O) optimized structural parameters of the ground (a^1A') and the lowest triplet excited state (ES) of $[Re(im)(CO)_3(dmp)]^+$. Experimental data are for $[Re(im)(CO)_3$(1,10-phenanthroline)$]^+$, taken from ref. (43).

Bond lengths, Å	Calc. a^1A'	Exp.[a] a^1A'	ES (UKS) Without symmetry	ES (UKS) C_S symmetry	ES(TDDFT) Without symmetry
Re-N7	2.172	2.182(4)	2.043	2.103	2.124
Re-N8	2.172	2.167(4)	2.155	2.103	2.124
Re-NE	2.190	2.185(5)	2.146	2.122	2.136
Re-C1	1.913	1.915(6)	1.963	1.988	1.957
Re-C2	1.911	1.907(6)	1.981	1.956	1.941
Re-C3	1.911	1.953(6)	1.981	1.956	1.941

References

1. Shih C*, et al.* (2008) Tryptophan-Accelerated Electron Flow Through Proteins. *Science* 320:1760-1762.
2. Takematsu K*, et al.* (2019) Two Tryptophans are Better than One in Accelerating Electron Flow Through a Protein. *ACS Cent. Sci.* 5:192−200.
3. Head-Gordon M, Grańa AM, Maurice D, & White CA (1995) Analysis of Electronic Transitions as the Difference of Electron Attachment and Detachment Densities. *J. Phys. Chem.* 99:14261-14270.
4. Cave RJ & Newton MD (1996) Generalization of the Mulliken-Hush treatment for the calculation of electron transfer matrix elements. *Chem. Phys. Lett.* 249:15-19.
5. Cave RJ & Newton MD (1997) Calculation of electronic coupling matrix elements for ground and excited state electron transfer reactions: Comparison of the generalized Mulliken–Hush and block diagonalization methods. *J. Chem. Phys.* 106:9213-9226.
6. Voityuk AA & Rösch N (2002) Fragment charge difference method for estimating donor–acceptor electronic coupling: Application to DNA π-stacks. *J. Chem. Phys.* 117:5607-5516.
7. Polák J, Ondo D, & Heyda J (2020) Thermodynamics of N‑Isopropylacrylamide in Water: Insight from Experiments, Simulations, and Kirkwood−Buff Analysis Teamwork. *J. Phys. Chem. B* 124:2495−2504.
8. Zhang Y, Liu C, Balaeff A, Skourtis SS, & Beratan DN (2014) Biological charge transfer via flickering resonance. *Proc. Natl. Acad. Sci. U.S.A.* 111:10049–10054.
9. Blumberger J (2015) Recent Advances in the Theory and Molecular Simulation of Biological Electron Transfer Reactions. *Chem. Rev.* 115:11191−11238.
10. Warshel A, Chu ZT, & Parson WW (1989) Dispersed Polaron Simulations of Electron Transfer in Photosynthetic Reaction Centers. *Science* 246:112-116.
11. Merrick JP, Moran D, & Radom L (2007) An Evaluation of Harmonic Vibrational Frequency Scale Factors. *J. Phys. Chem. A* 111:11683-11700.

12. Cailliez F, Müller P, Firmino T, Pernot P, & de la Lande A (2016) Energetics of Photoinduced Charge Migration within the Tryptophan Tetrad of an Animal (6−4) Photolyase. *J. Am. Chem. Soc.* 138:1904−1915.
13. Pižl M*, et al.* (2020) Time-Resolved Femtosecond Stimulated Raman Spectra and DFT Anharmonic Vibrational Analysis of an Electronically Excited Rhenium Photosensitizer. *J. Phys. Chem. A* 124:1253-1265.
14. Blanco-Rodríguez AM*, et al.* (2011) Phototriggering Electron Flow through Re^{I}-modified *Pseudomonas aeruginosa* Azurins. *Chem. Eur. J.* 17:5350 – 5361.
15. Takematsu K*, et al.* (2019) Hole Hopping Across a Protein-Protein Interface. *J. Phys. Chem. B* 123:1578−1591.
16. Ufimtsev IS & Martínez TJ (2009) Quantum Chemistry on Graphical Processing Units. 3. Analytical Energy Gradients and First Principles Molecular Dynamics. *J. Chem. Theor. Comp.* 5:2619-2628.
17. Berendsen HJC, Grigera JR, & Straatsma TP (1987) The Missing Term in Effective Pair Potentials. *J. Phys. Chem.* 91:6269-6271.
18. Heyda J*, et al.* (2009) Ion Specific Effects of Sodium and Potassium on the Catalytic Activity of HIV-1 Protease. *Phys. Chem. Chem. Phys.* 11:7599−7604.
19. Case DA*, et al.* (2015) AMBER 2014 (University of California, San Francisco).
20. Marenich AV, Jerome SV, Cramer CJ, & Truhlar DG (2012) Charge Model 5: An Extension of Hirshfeld Population Analysis for the Accurate Description of Molecular Interactions in Gaseous and Condensed Phases. *J. Chem. TheoryComput.* 8:527−541.
21. Maier JA*, et al.* (2015) ff14SB: Improving the Accuracy of Protein Side Chain and Backbone Parameters from ff99SB. *J. Chem. Theory Comput.* 11:3696–3713.
22. Ponder JW & Case DA (2003) Force Fields for Protein Simulations. *Adv. Prot. Chem. 66,* 66:27-85.
23. Cascella M, Magistrato A, Tavernelli I, Carloni P, & Rothlisberger U (2006) Role of protein frame and solvent for the redox properties of azurin from Pseudomonas aeruginosa. *Proc. Natl. Acad. Sci. U.S.A.* 52:19641–19646.
24. Berendsen HJC, Postma JPM, van Gunsteren WF, DiNola A, & Haak JR (1984) Molecular dynamics with coupling to an external bath. *J. Chem. Phys. 81,* 81:3684-3690.
25. Titov AV, Ufimtsev IS, Luehr N, & Martínez TJ (2013) Generating Efficient Quantum Chemistry Codes for Novel Architectures. *J. Chem. Theor. Comp.* 9:213-221.
26. Hay PJ & Wadt WR (1985) Ab initio effective core potentials for molecular calculations – potentials for K to Au including the outermost core orbitals. *J. Chem. Phys.,* 82:299-310.
27. Hehre WJ, Ditchfield R, & Pople JA (1972) Self—Consistent Molecular Orbital Methods. XII. Further Extensions of Gaussian—Type Basis Sets for Use in Molecular Orbital Studies of Organic Molecules. *J. Chem. Phys.* 56:2257-2261.
28. Adamo C & Barone V (1999) Toward reliable density functional methods without adjustable parameters: The PBE0 model. *J. Chem. Phys.* 110:6158-6170.
29. Adamo C, Scuseria GE, & Barone V (1999) Accurate excitation energies from time-dependent density functionl theory: Assessing the PBE0 model. *J. Chem. Phys.* 111:2889-2899.

30. Grimme S, Antony J, Ehrlich S, & Krieg H (2010) A consistent and accurate ab initio parametrization of density functional dispersion correction (DFT-D) for the 94 elements H-Pu. *J. Chem. Phys.* 132:154104.
31. Yanai T, Tew DP, & Handy NC (2004) A new hybrid exchange-correlation functional using the Coulomb-attenuating method (CAM-B3LYP). *Chem. Phys. Lett.* 393:51-57.
32. Ryckaert JP, Ciccotti G, & Berendsen HJC (1977) Numerical-Integration of Cartesian Equations of Motion of a System with Constraints - Molecular-Dynamics of N-Alkanes. *J. Comput. Phys.* 23:327−341.
33. Shao Y*, et al.* (2015) Advances in molecular quantum chemistry contained in the Q-Chem 4 program package. *Mol. Phys.* 113:184-215.
34. Lin B & Pettitt BM (2011) On the universality of proximal radial distribution functions of proteins. *J. Chem. Phys.* 134:106101
35. Frisch MJ*, et al.* (2016) Gaussian16, Revision A.03 (Gaussian, Inc., Wallingford, CT).
36. Levenberg K (1944) A Method for the Solution of Certain Non-Linear Problems in Least Squares. *Quart. Appl. Math.* 2:164-168.
37. Marquardt DW (1963) An Algorithm for Least-Squares Estimation of Nonlinear Parameters. *J. Soc. Ind. Appl. Math.* 11:431-441.
38. Reed AE, Weinstock RB, & Weinhold F (1985) Natural population analysis. *J. Chem. Phys.* 83:735-746.
39. Reed AE, Curtiss LA, & Weinhold F (1988) Intermolecular Interactions from a Natural Bond Orbital, Donor-Acceptor Viewpoint. *Chem. Rev.* 88:899-926.
40. Hirshfeld FL (1977) Bonded-atom fragments for describing molecular charge densities. *Theor. Chim. Acc.* 44:129–138.
41. Singh UC & Kollman PA (1984) An Approach to Computing Electrostatic Charges for Molecules. *J. Comput. Chem.* 5:129-145.
42. Bayly CI, Cieplak P, Cornell WD, & Kollman PA (1993) A Well-Behaved Electrostatic Potential Based Method Using Charge Restraints for Deriving Atomic Charges: The RESP Model. *J. Phys. Chem.* 97:10269-10280.
43. Connick WB, Di Bilio AJ, Hill MG, Winkler JR, & Gray HB (1995) Tricarbonyl(1,10-phenanthroline)(imidazole)rhenium(I): A Powerful Photooxidant for Investigations of Electron Tunneling in Proteins. *Inorg. Chim. Acta* 240:169-173.